

## Fluctuation microscopy: a probe of medium range order

This article has been downloaded from IOPscience. Please scroll down to see the full text article.

2005 Rep. Prog. Phys. 68 2899

(<http://iopscience.iop.org/0034-4885/68/12/R06>)

View [the table of contents for this issue](#), or go to the [journal homepage](#) for more

Download details:

IP Address: 68.3.77.237

The article was downloaded on 23/11/2010 at 22:02

Please note that [terms and conditions apply](#).

## Fluctuation microscopy: a probe of medium range order

M M J Treacy<sup>1</sup>, J M Gibson<sup>2</sup>, L Fan<sup>2</sup>, D J Paterson<sup>2</sup> and I McNulty<sup>2</sup>

<sup>1</sup> Arizona State University, Department of Physics and Astronomy, PO Box 871504, Tempe, AZ 85287-1504, USA

<sup>2</sup> Advanced Photon Source, Argonne National Laboratory, 9700 S. Cass Avenue, Argonne, IL 60439-4856, USA

Received 27 July 2005, in final form 8 August 2005

Published 10 October 2005

Online at [stacks.iop.org/RoPP/68/2899](http://stacks.iop.org/RoPP/68/2899)

### Abstract

Fluctuation microscopy is a hybrid diffraction-imaging technique that detects medium range order in amorphous materials by examining spatial fluctuations in coherent scattering. These fluctuations appear as speckle in images and diffraction patterns. The volume of material contributing to the speckle is determined by the point-spread function (the resolution) of the imaging optics and the sample thickness. The spatial periodicities being probed are related to the diffraction vector. Statistical analysis of the speckle allows the random and non-random (ordered) contributions to be discriminated. The image resolution that gives the maximum speckle contrast, as determined by the normalized variance of the image intensity, is determined by the characteristic length scale of the ordering. Because medium range ordering length scales can extend out to about the tenth coordination shell, fluctuation microscopy tends to be a low image resolution technique.

This review presents the kinematical scattering theory underpinning fluctuation microscopy and a description of fluctuation electron microscopy as it has been employed in the transmission electron microscope for studying amorphous materials. Recent results using soft x-rays for studying nanoscale materials are also presented. We summarize outstanding issues and point to possible future directions for fluctuation microscopy as a technique.

## Contents

	Page
List of acronyms	2901
1. Introduction	2901
1.1. Crystals, defects and disorder	2901
1.2. Medium range order in amorphous materials	2902
1.3. Microscopy methods for detecting medium range order	2903
1.3.1. The noise problem	2903
1.3.2. Extracting the signal from the noise	2905
1.3.3. Dark-field speckle imaging methods	2905
1.4. Fluctuation electron microscopy	2906
1.5. Paracrystallite model of amorphous silicon and germanium	2907
1.6. Extension of FEM to other disordered materials	2907
1.7. Microdiffraction methods	2909
1.8. Fluctuation x-ray microscopy	2909
2. Theory of scattering fluctuations	2910
2.1. Kinematical electron scattering theory	2910
2.2. Models of disorder and medium range order	2918
2.3. Computational models	2920
2.4. Experimental artefacts	2926
2.5. Ordering at longer length scales: choice of radiation	2928
3. Fluctuation electron microscopy of amorphous Si and Ge	2928
3.1. Evidence of medium range order	2928
3.2. Thermodynamic instability of paracrystallites	2929
3.3. Influence of substrate temperature on growth	2929
3.4. Effects of paracrystallite size, shape and orientation	2930
3.5. Amorphous silicon hydrogen materials	2931
3.6. Electron beam damage of quartz	2931
4. Extension to other radiations	2931
4.1. Fluctuation optical microscopy	2931
4.2. Fluctuation x-ray microscopy	2932
4.2.1. FXM of latex sphere packing	2932
4.2.2. Variable resolution FXM	2935
4.2.3. Dark-field x-ray microscopy	2936
5. Future directions and concluding comments	2937
5.1. Hardware and technique developments	2937
5.2. Disordered materials from the nanoscale to the mesoscale	2939
5.3. Conclusions	2941
Acknowledgments	2941
References	2941

## List of acronyms

CCD	Charge coupled device
CRN	Continuous random network
ECMR	Experimentally constrained molecular relaxation
FEM	Fluctuation electron microscopy
FOM	Fluctuation optical microscopy
FXM	Fluctuation x-ray microscopy
MRO	Medium range order
RDF	Radial distribution function
SEM	Scanning electron microscope
SRO	Short range order
STEM	Scanning transmission electron microscope
STXM	Scanning transmission x-ray microscope
TEM	Transmission electron microscope

## 1. Introduction

### 1.1. Crystals, defects and disorder

It has been observed that ‘Crystals are like people; it is the defects in them that tend to make them interesting’<sup>3</sup>. Although parallels between people and crystals should be greeted with great caution, this aphorism rings true for most microscopical studies of materials, particularly TEM, which tend to be motivated by a scientific interest in their defects. Traditionally, x-ray and neutron diffraction have been the methods of choice for unravelling the structures of perfect crystals, whereas TEM has been the method of choice for probing their deviations from crystalline perfection, being capable of both diffraction and imaging at atomic resolution. However, with the advent of efficient x-ray focusing systems, such as Fresnel zone plates [1,2,105], or simply the use of micron size pinholes to raster a sample, the ability to image with x-rays at the nanometre scale has opened up new possibilities for exploring defects in nanomaterials.

In general terms, the concepts of order and disorder are quite complex and a detailed discussion is beyond the scope of this review. Ossi [3] gives a nice summary of the issues behind these concepts. For example, many of the drawings by Escher eloquently reveal the distinction between order and regularity. In fluctuation microscopy, we are concerned with spatial arrangements of atoms or nanoparticles and how those arrangements coherently scatter incident radiation.

Because of translational periodicity and symmetry, crystalline order is relatively easy to describe efficiently. Ignoring thermal motions, unit cells obey a strict translational invariance and are thus considered regular. Within each unit cell, space group symmetry operations describe how an asymmetric motif, or basis arrangement of points, can be mirrored, rotated and translated to tile the unit cell. The translational periodicity of the crystal defines a lattice that, for a primitive unit cell, can be conveniently taken to be the locations of the unit cell corners. A crystalline material can then be viewed as being built with reference to an idealized crystallographic lattice. The success of x-ray and neutron diffraction studies of crystalline materials is predicated on the assumption that there is an underlying crystallographic space group type that defines the lattice. The problem of structure determination is then efficiently

<sup>3</sup> This statement has been attributed variously to F C Frank, C J Humphreys and J M Thomas. The earliest reference the authors could locate in print is J M Thomas, *Chemistry in Britain* (1970).

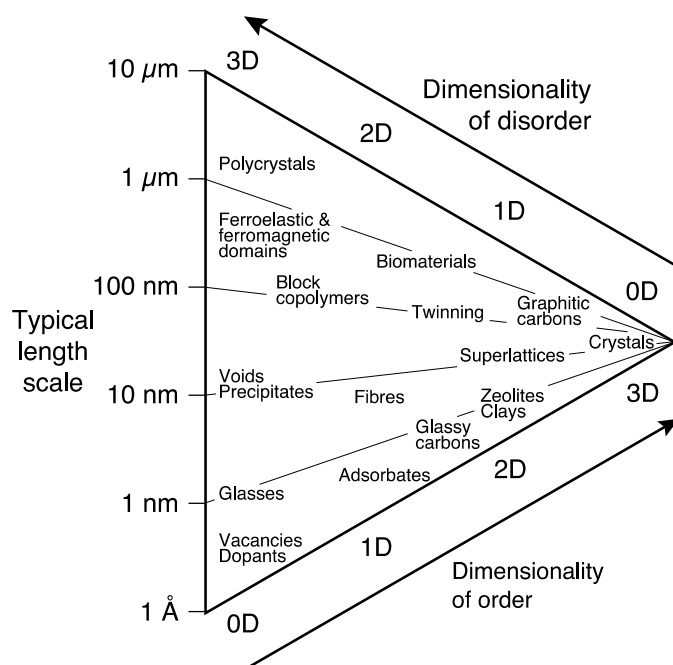


**Figure 1.** Typical length scales and dimensionality of disorder in some classes of materials. The disorder in most materials is usually defined relative to a lattice. Glasses are an exception, where short range order is determined by nearest neighbour bond distances and interbond angles. Medium range order in glasses refers to residual correlations between atom positions on length scales between 0.5 and 3 nm.

reduced to that of determining the types and locations of an asymmetric unit of atoms, the unit cell dimensions and a space group type.

Crystal defects are generally viewed as perturbations to the lattice. Figure 1 broadly summarizes the types of disorder found in many materials. The figure is not intended as a pedagogical summary of all types of disorder but as a broad overview of the types of static structural disorder that are frequently encountered. Materials may be classified approximately according to the dimensionality of the order (bottom axis), or conversely, the dimensionality of the disorder (top axis) and the associated typical length scales. Disorder in these materials can be viewed as a form of spatial noise, where atoms are statically displaced from an ideal lattice. Phonons also introduce displacements from the lattice, and represent temporal noise, with atoms vibrating stochastically about lattice points. Gases and liquids also have significant temporal noise, since atom locations are not fixed. Temporal fluctuations in atomic positions are of great interest in materials science, and in principle can be studied by fluctuation microscopy, but are not considered in this paper. Fluctuation microscopy is a spatial-domain analogue of photon correlation spectroscopy (also called intensity fluctuation spectroscopy or dynamic light scattering), which examines variations in the temporal fluctuations of light scattered by a sample. As is true for most scattering techniques, the incident radiation for fluctuation microscopy could be visible light photons, x-ray photons or other particles such as electrons.

### 1.2. Medium range order in amorphous materials

Glasses and amorphous materials exhibit an extreme form of disorder, and deviate somewhat from the lattice paradigm, since it no longer makes sense to define their structures relative to

a lattice. There is no long-range order. However, in a densely packed solid, atom positions cannot be truly random since no two atoms can be closer than a typical bonding distance. Consequently, there can be significant short-range order. Such short-range order can be efficiently studied by x-ray, neutron and electron diffraction methods [4–7]. For example, the RDF, which is the spherically-averaged atom pair distribution, generally shows a fairly sharply defined first nearest neighbour peak, with peaks due to next nearest neighbours quickly broadening out at pair separations of around 1 nm, beyond which little correlation is evident. Recent advances using high resolution spectrometers in conjunction with high brightness coherent synchrotron radiation sources indicate that this range could be extended [5, 6, 8–10].

It was proposed by Zachariassen [11] that amorphous tetrahedral semiconductor materials adopt a CRN structure, that retains the 4-coordinated bonding, has low bond strain energy but no periodic ordering (i.e. long range order). Correlations at the 3 nm atomic length scale and longer correspond to polycrystallinity or long range ordering and are relatively easy to detect in both diffraction and by transmission electron microscopy imaging methods. Correlations within the range of length scales 0.5–3.0 nm correspond to medium range order. The experimentally tricky range 1–2 nm has been notoriously elusive to ordinary diffraction and imaging methods, mainly because the coherent diffraction signal is weak and tends to be lost against the background signal.

### 1.3. Microscopy methods for detecting medium range order

**1.3.1. The noise problem.** The quest to detect and characterize medium range order in amorphous materials has a relatively long history. Given the ability of TEM to resolve single atom columns in thin materials, it was surmized early on that TEM imaging should be an ideal method for seeing medium range order in amorphous materials [12, 13]. It seemed reasonable that high resolution bright field imaging should straightforwardly reveal nanocrystallites embedded in thin films. The nanocrystallites would show up as small patches of regular lattice fringes in the images. Although simple in concept, this method turned out to be problematic, mainly because of pattern recognition artefacts in noisy backgrounds. An illustration of this problem is shown in Figure 2. Figure 2(a) shows a high resolution TEM bright field image of a thin ( $\sim 4.5$  nm thick) amorphous silicon sample. It was taken in a JEOL 4000 EX at 400 keV, at an objective lens defocus of  $\Delta f = -90$  nm. The image shows many small patches containing 2 or 3 fairly evenly spaced features or fringes. Image contrast is sensitive to the exact microscope imaging conditions, and small changes in objective lens defocus can change the character of an image significantly. Figure 2(c) shows the same region imaged at a defocus of  $\Delta f = -120$  nm. This image is quite different from figure 2(a) and exhibits pronounced patches containing regularly spaced features. However, as shown originally by Krivanek *et al* [14], the impression of local ordering is largely illusory. Figure 2(b) is the same image as shown in figure 2(a), except that the phases of the image Fourier components have been randomized by computer processing. Remarkably, the image is qualitatively unchanged. Similarly, figure 2(d) is the same as 2(c), except for the phase randomization. Figure 2(d) preserves the strong fringiness of figure 2(c). The fringiness is mostly an artifact of the objective lens band pass filtering (or contrast transfer function) and has little relationship with any local ordering in the sample.

Another example of the illusory nature of local structure in images is given in figure 3. This is a TEM image simulation of an artificial ‘sample’ that is simply an image array of pixels whose values are set randomly between 0 and 255 (figure 3(a)). After processing this array with an image bandpass filter corresponding to the JEOL 4000 EX at 400 keV (figure 3(b)), the resultant image is distressingly similar to the image of amorphous silicon in Figure 2(a). However, it

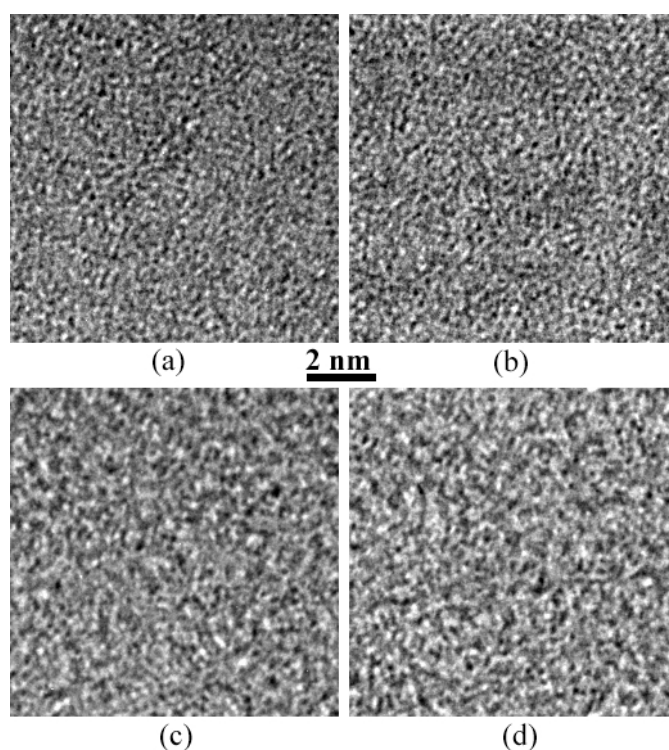


**Figure 2.** (a) Bright field TEM image of a thin evaporated amorphous Si sample, taken at an objective lens defocus of  $\Delta f = -90$  nm. (b) The same image after randomizing the phases in Fourier space. The image is qualitatively identical, even though the information has been scrambled. (c) Bright field TEM image of the same sample area, taken with an objective lens defocus of  $\Delta f = -120$  nm. The image appears to show pronounced short-range ordering. (d) The same image after randomizing the phases in Fourier space. Again, the image is qualitatively identical, even though the information has been scrambled. The appearance of order in the original data of (a) and (c) is largely illusory.

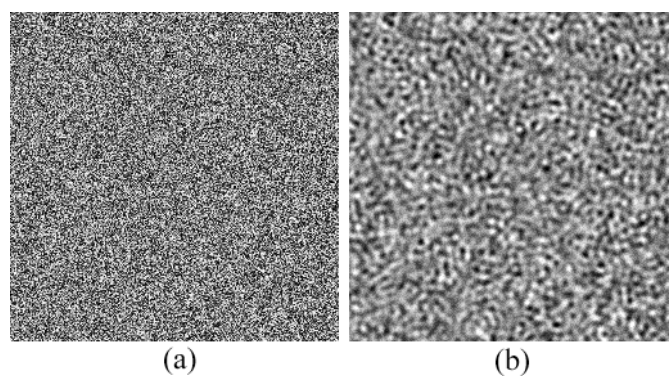


**Figure 3.** (a) Image array of pixels whose values are set randomly between 0 and 255. (b) The same array after being processed by a typical TEM image bandpass filter. The resultant image is qualitatively similar to images of amorphous silicon.

would be going too far to say that images of amorphous materials are indistinguishable from random arrays of points. Structural information, projected through the sample thickness, is undoubtedly present in Figure 2(a), but is weak against the averaged background.

*1.3.2. Extracting the signal from the noise.* Occasionally, the signal-to-noise may be strong enough to allow direct processing of images. An interesting example is the work of Cheng *et al* [15] who studied thin films of ion-implanted amorphous Si. They found that by cross-correlating images with the expected image projection of a small Si particle oriented with the [110] direction parallel to the beam, and progressively rotated in azimuth, a statistically significant number of [110]-oriented Si nanoclusters were found. They showed that the density of Si nanoclusters decreased as a function of post-implantation annealing temperature. The success of this experiment relied on the ability to obtain thin films with minimal sample-thinning surface artefacts, whose thickness is only a few multiples of the characteristic Si crystallite size. When the sample is too thick, the signal from individual crystallites becomes lost against the increased background projection of amorphous Si or of other Si grains above or below in different orientations.

Direct bright field TEM imaging has been shown to give useful information about graphitic ordering in amorphous carbons [14, 16, 17]. Graphitic and polyaromatic fragments, longer than 3 nm, can be detected in bright field images when they align edge-on to the beam. Such samples contain long, narrow and frequently serpentine, image features. While the precise structural details of these features are uncertain, the image technique is robust enough to allow comparative studies between samples. This method has been used to conduct interesting studies of terrestrial and extra-terrestrial carbons [18, 19].

It was recognized early on that when the signal-to-noise is weak in TEM images, a statistical approach may be a useful compromise for extracting averaged structural information [20, 21]. Fan and Cowley [22] addressed the problem from an information-theoretic viewpoint in an effort to isolate the non-random image features in bright field images of amorphous carbon. They concluded that the technique was too sensitive to the oscillatory nature of the microscope point-spread function. Nevertheless, this seems to be a promising approach.

*1.3.3. Dark-field speckle imaging methods.* It was conjectured by Rudee and Howie [23] that the speckle observed in dark field images of amorphous materials reveals underlying structural order, particularly the presence of microcrystallites imbedded in an amorphous matrix. Whereas bright-field images are fraught with phase contrast artefacts, as discussed above, dark-field images are dominated by amplitude contrast mechanisms and therefore should reveal coherently scattering regions more reliably. A typical tilted dark-field speckle image from a 23 nm thick film of amorphous Ge is shown in figure 4. It is naturally tempting to conclude that some of the brighter (or darker) speckles are coherently diffracting ordered regions. Bright regions are due to constructive interference; darker regions are due to destructive interference. However, it was pointed out by Chaudhari and Graczyk [24, 25] that dark-field image speckle cannot be interpreted too literally. Speckle can arise because of coherent scattering from random atomic alignments, as well as from structurally correlated alignments. Thus, the presence of speckle in a dark field image is not necessarily an indication of structurally coherent regions (i.e. microcrystallites). This means that individual speckles (both bright and dark patches) in figure 4 cannot be interpreted literally as microcrystallites. There may be microcrystallites present—we just cannot say which ones. This ambiguity introduced by chance atom alignments hampered the effective use of the dark-field speckle technique, since the mere presence of speckle is not a definitive indicator of short-range, or



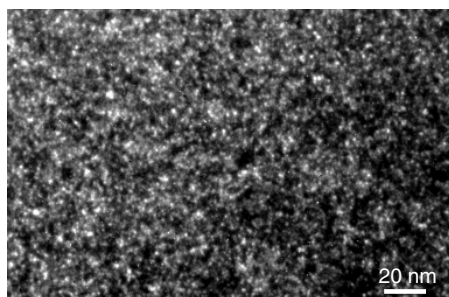


**Figure 4.** Tilted dark field TEM image of 23 nm thick amorphous germanium showing speckle.

medium-range, order in amorphous materials. Nevertheless, the dark field speckle idea was followed up by a number of other promising studies. An interesting development was the use of hollow cone illumination to generate the speckle. Instead of an illuminating beam at a fixed declination and azimuthal angle, as in standard tilted dark-field, hollow cone illumination irradiates the sample over the full  $360^\circ$  azimuthal tilt angle [26, 27]. The idea was that since the hollow cone illumination is spatially incoherent in azimuth, the speckle contributions from random alignments between neighbouring columns of atoms would be suppressed. It was conjectured that the suppression of the random speckle contribution would allow the contribution from microcrystallites to be more easily detected [28, 29]. The hollow cone method was indeed found to suppress speckle, compared with tilted dark-field illumination, and the technique was shown to be capable of detecting extended ( $\geq 2$  nm diameter) graphitized regions in thin amorphous carbons.

Although the use of incoherent hollow cone dark-field illumination went a long way towards suppressing the random coherent scattering, it was recognized early on that in order to detect medium range order reliably against a background of structurally random speckle quantitative statistical methods were needed. Although some quantitative studies were made [31, 30] using digitized electron micrograph data, the early technology was too cumbersome for routine use, and results were inconclusive.

#### 1.4. Fluctuation electron microscopy

With the introduction of efficient slow-scan CCD cameras and fast inexpensive computers to collect the data, quantitative real-time analysis of electron micrographs became possible. With such technology available, follow-up studies with hollow cone dark-field in the TEM showed that statistical measurements of dark field speckle can detect medium range order. Treacy and Gibson [32–34] showed that the image speckle from evaporated amorphous Si and Ge films can change qualitatively when the hollow cone angle changes. Figure 5 shows four images of thin ( $\sim 14.4$  nm thick) amorphous Ge taken at different hollow cone angles. The image intensities have been adjusted so that they all have the same mean intensity, but the relative contrasts have not been altered. The speckle has maximum amplitude in figure 5(d) at hollow cone tilt corresponding to  $q = 35.8 \text{ nm}^{-1}$ . The speckliness of an image can be estimated from the image intensity variance. This works well provided there are no sample thickness, composition or illumination intensity gradients across the image. The variance, when normalized by the square of the mean image intensity, to eliminate the intensity drop-off due to the germanium atomic form factor allows the relative speckliness as a function of hollow cone tilt angle to be compared. By plotting the normalized image intensity variance as a function of tilt angle, Treacy and Gibson showed that the speckliness has two pronounced broad maxima. The first

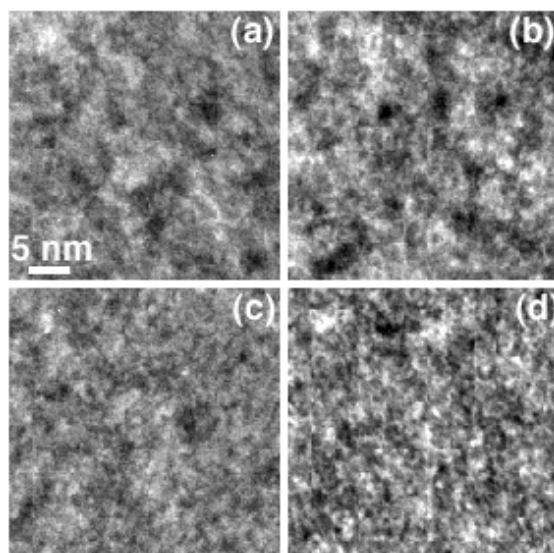


**Figure 5.** Hollow cone dark field images of 14.4 nm thick amorphous Ge as a function of scattering vector amplitude  $q$ . (a)  $q = 15.7 \text{ nm}^{-1}$ , (b)  $q = 18.8 \text{ nm}^{-1}$ , (c)  $q = 26.7 \text{ nm}^{-1}$ , (d)  $q = 35.8 \text{ nm}^{-1}$ . The speckle varies as a function of  $q$ , being most pronounced at  $q = 35.8 \text{ nm}^{-1}$ , revealing that the underlying atomic structure is not random.

peak is at a scattering angle corresponding to the cubic germanium {111} and the second spans the {220} and {311} reflections (figure 6). They also showed that the normalized variance is reduced when the sample is annealed (*in situ*) to 350 °C, which is below the recrystallization temperature. The peaks in normalized variance were interpreted as a signature of medium range order because (i) the speckle from random atomic alignments is not expected to exhibit a strong dependence on scattering angle (hollow cone tilt  $q$ ) and (ii) the fact that the speckliness can be reduced significantly by annealing the sample, whereas the diffracted intensities are essentially unchanged.

### 1.5. Paracrystallite model of amorphous silicon and germanium

It was argued that the reduction of speckle indicates a reduction in medium range order, and that the annealing transformed the sample more towards the CRN. It was conjectured that the as-deposited amorphous evaporated germanium is a compact of paracrystallites, which are 1–2 nm diameter particles with the cubic Ge bonding topology, but are highly strained. This combination of small size and strain probably tends to make them ‘diffraction amorphous’, but they are still revealed at the statistical level in the dark-field speckle images. Thin films of evaporated amorphous silicon were also shown to contain similar paracrystallites.

Comprehensive FEM studies of many different types of amorphous Si (and amorphous Si:H) have found that paracrystallites are pervasive and not unique to evaporated thin films [35–38].

### 1.6. Extension of FEM to other disordered materials

Since those original studies on amorphous silicon and germanium, FEM has been applied fruitfully to the study of other types of disordered materials. Chen *et al* [39–41] have

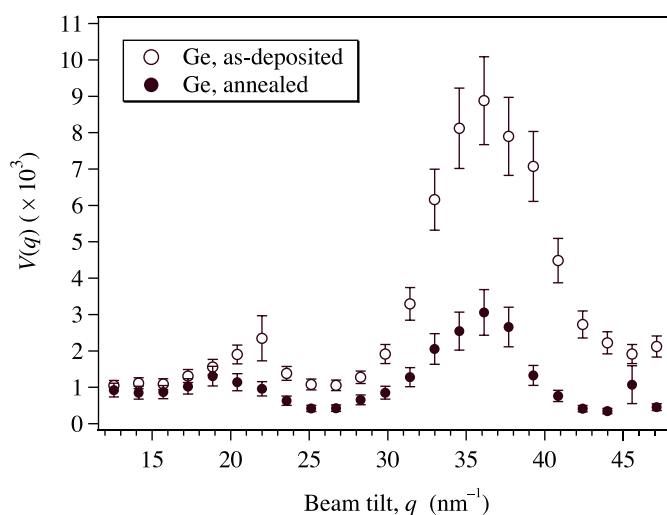


**Figure 6.** Normalized variance  $V(q, K_{\text{ap}})$  versus  $q$  for 14.4 nm thick evaporated Ge film. The objective aperture acceptance semi-angle was equivalent to  $K_{\text{ap}} \approx 26 \text{ nm}^{-1}$ . Open circles are for the as-deposited Ge film. Filled circles are for the annealed film (Data from [32]).

studied amorphous diamond-like (mostly 4-coordinated) carbon materials and shown that medium range ordering is present at length scales exceeding 1 nm. Upon annealing, they succeeded in tracing the evolution of graphitic (3-coordinated) regions in their samples. In a related study on hydrogenated near-frictionless carbon films, Johnson *et al* [42] found that the extent of medium range order correlates with the coefficient of friction of these films.

Metallic glasses have also been studied, although as alloys they are inherently more complicated structurally than the elemental silicon and germanium tetrahedral semiconductors. In their annealing studies of quenched  $\text{Al}_{92}\text{Sm}_8$  alloys, Stratton *et al* [43–45] found nanoscale medium range ordering of the Al that decreased as annealing temperature increased. However,  $\text{Al}_{92}\text{Sm}_8$  materials that were disordered by intense mechanical deformation did not show any medium range order. Hufnagel and colleagues [46, 47] have shown that the sample thinning methods used to make TEM samples can have a large effect on the apparent presence of order and disorder. They also showed that relatively minor changes in alloy composition can have a large effect on the medium-range order, and that changes in medium range order are correlated with changes in mechanical behaviour. Shear bands in Zr-based metallic glasses have also been studied by FEM [46, 48]. Again, medium range order was found to be sensitive to the alloy composition.

Oxide glasses have also been examined. Chen *et al* [49] showed that amorphous  $\text{Al}_2\text{O}_3$  passivation layers are more susceptible to penetration and corrosion after exposure to  $\text{Cl}^-$  anions because of structural changes in the  $\text{Al}_2\text{O}_3$  layers. High- $K$  amorphous  $\text{HfO}_2$  dielectric materials were found to possess a high degree of medium range order depending on the growth conditions [50]. In a study of electron beam irradiation damage in quartz, Cheng *et al* [51, 52] found no traces of residual medium range order in the amorphized  $\text{SiO}_2$  regions, even within a few nanometres of the growing amorphous/crystalline boundary. However, nanometre-sized Si particles were found to precipitate into the amorphous  $\text{SiO}_2$ , presumably because trace amounts of oxygen are liberated by the beam damage process [53].

### 1.7. Microdiffraction methods

Fluctuation microscopy is not the only microanalysis technique for exploring changes in local order. Microdiffraction methods, from electron probes as narrow as 0.1 nm, can efficiently explore the ordering within local projections through a sample. Cowley [54–56] and Rodenburg [57] have used electron microdiffraction methods to study structural correlations in amorphous carbon and silicon in detail. Voyles and Muller [58] demonstrated how correlation length scales in amorphous Si can be explored by varying the probe size in a STEM—the so-called *variable resolution microscopy* [59]. Earlier attempts to implement variable resolution microscopy, using a continuously adjustable square objective aperture in a TEM, failed because of engineering difficulties with the aperture [60]. Cowley [56] demonstrated a form of variable resolution microscopy by examining speckle in microdiffraction patterns as a function of probe defocus. In an important advance, McBride and Cockayne [61, 62] have demonstrated that microdiffraction from very thin samples, after deconvolution for the probe convergence by Lucy–Richardson methods, can be used to determine local RDFs in disordered materials from volumes as narrow as  $\sim 2$  nm.

### 1.8. Fluctuation x-ray microscopy

While the number of groups actively using fluctuation microscopy as a technique appears to be growing steadily, there have also been advances in the development of a synchrotron soft x-ray ( $\lambda \approx 0.7$  nm) analogue of the technique, FXM [63, 64]. Experiments indicate that fluctuation microscopy is well suited for detecting medium range order in disordered materials at length scales  $L$  between  $2 \leq L/d \leq 15$ , where  $d$  is the characteristic spacing of structural units in the material (e.g. interatomic bond lengths). Whereas the TEM-based fluctuation microscopy is well suited for studying medium range order at the atomic scale ( $\geq 0.5$  nm), the x-ray based fluctuation microscopy is better suited to studying ordering within self-assembled nanoscale materials ( $\geq 5$  nm).

Fluctuation microscopy as a technique has acquired a number of names over the years that all refer essentially to the same technique. The earliest name would be *dark-field speckle imaging*. The hollow cone dark-field speckle imaging technique was termed *variable coherence microscopy*, because the hollow cone tilt angle controls the coherence volume of the scattering geometry. A variant method was called *variable resolution microscopy*, where, instead of the tilt angle, it is the objective aperture width that is varied, which in turn controls the width of the sample volumes that can contribute to the speckle. Since the speckle in dark field images arises because of structural fluctuations between neighbouring sample volumes, such dark field speckle techniques in the TEM became known collectively as FEM. The fluctuations, of course, are spatial and not temporal.

Having provided an overview of the origins of fluctuation microscopy, in the following sections we will examine the technique in more detail. We will present the kinematical scattering theory of FEM, explaining why it is sensitive to medium range order (MRO). To illustrate how FEM works in practice, we will describe in more detail some of the earlier FEM experiments on thin films of amorphous silicon and germanium. Since the principles of fluctuation microscopy are not restricted to electron scattering, we will also describe recent FXM experiments on self-assembled nanoscale materials. Because fluctuation microscopy is still emerging as a technique, we will also discuss future directions, both in terms of materials that could be usefully probed by the fluctuation microscopy methods and also possible developments in both hardware and theory.

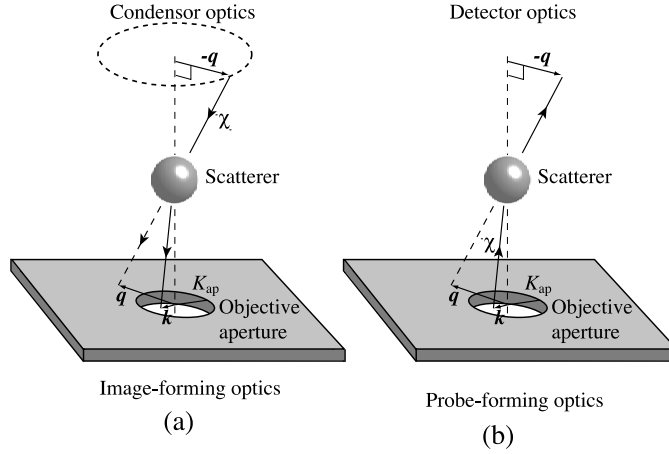


**Figure 7.** Diagram showing the sample scattering geometry in its simplest form. (a) Conventional TEM imaging geometry with illumination incident from a condenser system, and the scattering being collected by an objective aperture. The radiation that passes through the aperture is then gathered and focused by post-specimen imaging optics to form an image. (b) Scanned probe imaging geometry. A probe is formed by the objective aperture and probe-forming lenses. The scattering is then collected by detectors. According to the reciprocity principle, these two geometries give equivalent information about the sample, provided the probe is scanned over the sample.

## 2. Theory of scattering fluctuations

### 2.1. Kinematical electron scattering theory

We wish to model the variations in the scattering of incident radiation between small sub-volumes of a static assembly of objects. The fluctuations we are interested in are these spatial variations in scattered intensity. We assume that the scattering is kinematical—that is, it is weak compared with the incident intensity, and multiple scattering can be ignored. We consider the radiation that is transmitted through the sample, which is presumed to be thin; what is meant by thin depends on the scattering factors. For amorphous Si samples in the TEM, this usually means that the thickness needs to be less than about 100 atoms, or about 25 nm, for 100 keV electrons.

The specimen is treated as an assembly of scatterers  $j$  at positions  $\mathbf{r}_j$ . The sample is illuminated by plane wave radiation of wavelength  $\lambda$ , and associated wavevector amplitude  $\chi = 2\pi/\lambda$ , that is inclined to the optic axis by an amount  $-q$  (see figure 7(a)). This corresponds to an illumination tilt angle of  $\sin^{-1}(|q|/\chi)$ , which is approximately  $|q|/\chi$  for small  $|q|$ . The radiation is scattered by the object into an outgoing plane wave that is inclined to the optic axis by an amount  $k$ . The amplitude of the scattered wave far from the sample is

$$\phi_j(\mathbf{r}', \mathbf{r}_j, \mathbf{q}, \mathbf{k}) = i\lambda f_j(|\mathbf{k} - \mathbf{q}|) e^{-i(\mathbf{k} - \mathbf{q}) \cdot \mathbf{r}_j} e^{i\mathbf{k} \cdot \mathbf{r}'}, \quad (1)$$

where  $f_j(|\mathbf{k} - \mathbf{q}|)$  is the scattering factor of the object for scattering at  $\mathbf{k} - \mathbf{q}$  and  $\mathbf{r}'$  is a spatial coordinate in the far-field. Note that, for consistency, both the  $\mathbf{q}$  and  $\mathbf{k}$  vectors are referenced to the same plane (here it is the back focal plane of the objective aperture). With this convention, the condition  $\mathbf{k} = \mathbf{q}$  corresponds to a zero deflection of the incident beam (see figure 7). In order to be more consistent with standard nomenclature for x-ray scattering, we have reversed the meaning of the vectors  $\mathbf{q}$  and  $\mathbf{k}$  relative to our earlier publications [26, 33]. In addition, here the vector amplitudes  $q$  and  $k$  are related to real-space spacings  $d$  through  $q \equiv 2\pi/d$ ,

whereas in earlier electron microscopy papers we had used  $q \equiv 1/d$ , a convention that is more commonly encountered in electron microscopy scattering theory.

For image formation, the scattering collected by an objective aperture of radius  $K_{\text{ap}}$  is focused at a plane in the far-field that is conjugate with the sample. The image wave function  $u_j$  of scatterer  $j$  is given by the coherent sum of the scattered plane waves that are collected by the aperture:

$$u_j(\mathbf{r}', \mathbf{r}_j, \mathbf{q}, K_{\text{ap}}) = \iint_{\text{obj}} \phi_j(\mathbf{r}', \mathbf{r}_j, \mathbf{q}, \mathbf{k}) d^2\mathbf{k} \quad (2)$$

or

$$u_j(\mathbf{r}, \mathbf{r}_j, \mathbf{q}, K_{\text{ap}}) = i\lambda e^{iq \cdot \mathbf{r}_j} \iint_{\text{obj}} f_j(|\mathbf{k} - \mathbf{q}|) e^{i\mathbf{k} \cdot (\mathbf{r} - \mathbf{r}_j)} d^2\mathbf{k}. \quad (3)$$

For dark-field imaging,  $|\mathbf{q}| > K_{\text{ap}}$  since the unscattered illumination does not enter the objective aperture.

In a microscope, the image is usually magnified. Here, for convenience we have sidestepped the issue of magnification by mapping the far-field coordinate  $\mathbf{r}'$  back onto the sample plane (or, equivalently, by mapping the sample coordinate  $\mathbf{r}_j$  onto the far-field). This is legitimate because the image plane and sample plane are mutually conjugate. Thus, in equation (3)  $\mathbf{r}$  and  $\mathbf{r}_j$  can both be considered to be in sample coordinates, sharing the same scaling.

Microscope lenses are seldom perfect, introducing aberrations that perturb the phases of the constituent plane waves arriving at the image plane. Lens aberrations will modify equation (3) to

$$u_j(\mathbf{r}, \mathbf{r}_j, \mathbf{q}, K_{\text{ap}}) = i\lambda e^{iq \cdot \mathbf{r}_j} \iint_{\text{obj}} f_j(|\mathbf{k} - \mathbf{q}|) e^{i\mathbf{k} \cdot (\mathbf{r} - \mathbf{r}_j)} e^{i\gamma(|\mathbf{k}|)} d^2\mathbf{k}, \quad (4)$$

where

$$\gamma(|\mathbf{k}|) = \pi\lambda|\mathbf{k}|^2[\Delta f + \frac{1}{2}C_s\lambda^2|\mathbf{k}|^2]. \quad (5)$$

$\Delta f$  is the ‘defect of focus’, or defocus, of the lens and  $C_s$  is the coefficient of spherical aberration. Astigmatism and higher order aberration terms are also present, but are usually less important in FEM experiments, which are usually conducted at low resolution. Chromatic aberrations can be important, but are ignored here because we assume for simplicity that we have monochromatic radiation. Strictly speaking, the precise value of defocus,  $\Delta f$ , depends not just on the lens strength but also on the height of each scatterer within the sample. This correction is important only at high resolutions when the depth of focus is short relative to the specimen thickness and is ignored here.

For low resolution imaging, where individual scatterers are not resolved, we can introduce the approximation that

$$u_j(\mathbf{r}, \mathbf{r}_j, \mathbf{q}, K_{\text{ap}}) = f_j(|\mathbf{q}|) a_j(\mathbf{r} - \mathbf{r}_j, K_{\text{ap}}) e^{iq \cdot \mathbf{r}_j}, \quad (6)$$

where

$$a_j(\mathbf{r} - \mathbf{r}_j, K_{\text{ap}}) = i\lambda \iint_{\text{obj}} e^{i\mathbf{k} \cdot (\mathbf{r} - \mathbf{r}_j)} e^{i\gamma(|\mathbf{k}|)} d^2\mathbf{k}. \quad (7)$$

The validity of the decomposition in equation (6) depends on the validity of the assumption that the scattering factor  $f_j(|\mathbf{k} - \mathbf{q}|)$  can be treated as constant for the range of  $\mathbf{k}$  subtended by the objective aperture and taken outside of the integral in equation (4). This is the ‘incoherent’ imaging approximation, which works well in dark field TEM imaging for resolutions down to 0.1 nm. It is equivalent to assuming that each scatterer is effectively a point compared

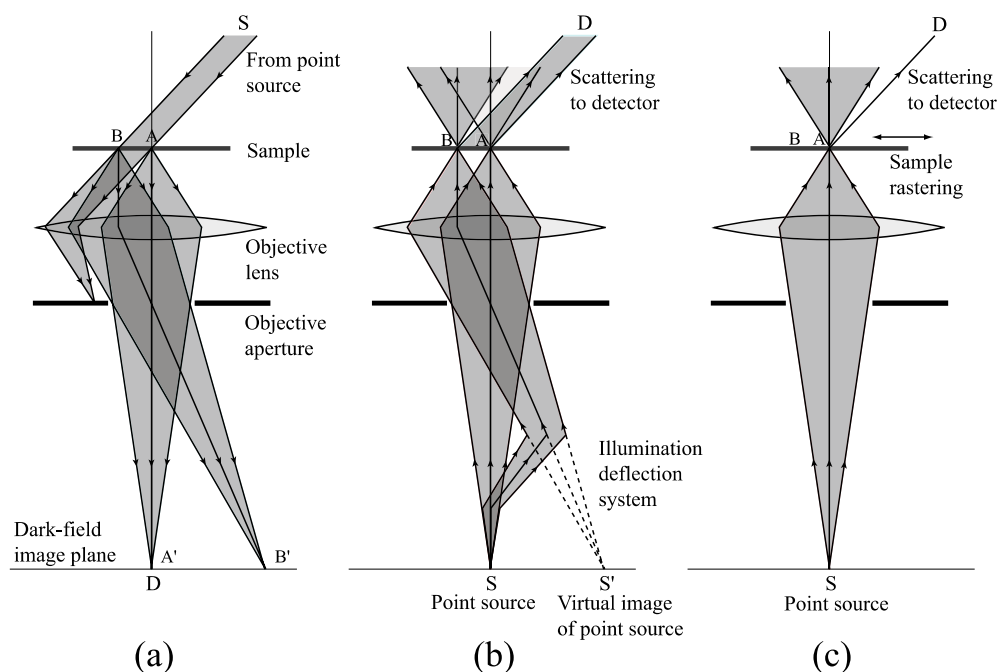


**Figure 8.** Schematic representations of several experimental transmission imaging configurations. (a) Fixed illumination. The illumination originates at the top (source S), is scattered by the specimen and then collected and focused by the objective lens to form an image at the conjugate plane at the bottom. Intensity is sampled by a point detector D. This is equivalent to the conventional TEM. (b) Scanned probe. The illumination originates at S, which is now shown at the bottom, and is focused onto the sample by an objective lens. The scattering is collected at the top by a point detector D. This is equivalent to the STEM. (a) and (b) are drawn so that their relationship through the reciprocity principle is clear. Note that S and D are swapped between these two figures, and the direction of the radiation is reversed. (c) Scanned sample. This is equivalent to (b), but here the sample is rastered. This is equivalent to the mode of operation of a STXM.

with the resolution of the image, which is determined by the point-spread function. The function  $a_j(\mathbf{r} - \mathbf{r}_j, K_{\text{ap}})$  represents the amplitude of the point-spread function of the optical system, at position  $\mathbf{r}$ , when centred on atom  $j$ . For x-ray and optical imaging of assemblies of nanoscale particles, the scattering factors of such particles can be oscillatory. However, for small apertures (low resolution) whose width  $K_{\text{ap}}$  is much smaller than the oscillation period, this approximation has been shown to be robust [32].

There are two equivalent ways to acquire images in a microscope. The fixed illumination method irradiates the sample with a well-defined source, and the scattering is gathered and magnified by an objective lens and projected (and possibly further magnified by a set of projection lenses) onto an image plane (see figure 8). As noted above, the image and sample planes are conjugate. The image differs from the sample in that it is magnified and filtered by the imaging system, the most important element of which is the objective lens and its aperture. The scanning method irradiates the sample on a point-by-point basis by using the objective lens to form a finely focused probe on the sample. Detectors then collect the scattering. Images are built up either by rastering the probe over the sample (figure 8(b)) or by physically moving the sample itself across a fixed focused probe (figure 8(c)) and displaying the collected signals as a two-dimensional intensity array that matches the pixilation of the scan. Scanning, and scanning transmission, electron microscopes usually scan the sample by deflecting the electron



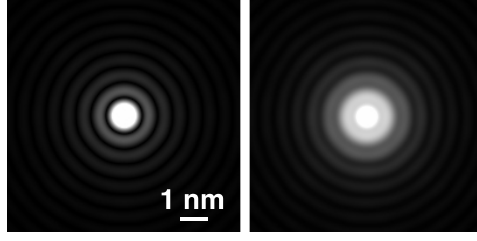


**Figure 9.** Resolution functions  $a_j$  for an aperture  $K_{\text{ap}} = 7.5 \text{ nm}^{-1}$ , radiation wavelength  $\lambda = 3.7 \text{ Pm}$ . On the left, defocus = 0 nm. On the right, defocus = 50 nm.

beam using magnetic coils or electrostatic deflectors. Scanning optical and x-ray microscopes usually scan by moving the sample.

In principle, the two types of image acquisition methods, fixed illumination of figure 8(a), or the scanning methods of figures 8(b) and 8(c), can produce identical images. The Helmholtz reciprocity principle [65] asserts that if a point source S and a point detector D exchange positions, then if the source emitted wave function has not changed, the detected wave function will also be unchanged. The reciprocity principle does not claim, however, that swapping the source and detector will produce identical images at the detector plane. The equivalence of wave functions applies only to two points within the system, S and D. Equivalent images are obtained, after swapping, by scanning the swapped source S over the original image plane and monitoring the detected signal at D, to build up the image point by point.

The function  $a_j$  can therefore be interpreted in two equivalent ways. For fixed illumination imaging,  $a_j^2$  is the point-spread function of the microscope, defining the image resolution. For a scanned probe,  $a_j^2$  is the probe intensity profile, which defines the probed sample width and the resolution of the scanned image.

In fluctuation microscopy we are interested in the variations in scattering between sample sub-volumes. The resolution function  $a_j$ , in conjunction with the local sample thickness  $t$ , conveniently delineates such sub-volumes. If for simplicity we approximate the resolution function  $a_j$  by a simple ‘top-hat’ type of function with a uniform amplitude and phase across a width  $W$ , and zero intensity beyond, then the sampled volume is simply a cylindrical region with volume  $\pi W^2 t / 4$ . However, for a perfectly focused lens, the resolution function is better modelled as an Airy disc, with an oscillatory decaying amplitude with increasing distance from the centre, as shown in figure 9. Thus, in practice, the actual sampled volume is not a uniform contiguous chunk of the specimen. The contribution of an individual scatterer  $j$  to the final scattered intensity is weighted by the local amplitude and phase of  $a_j$  which, in turn, are governed by the objective aperture radius  $K_{\text{ap}}$  (generally, larger  $K_{\text{ap}}$  gives a narrower  $a_j$ ) and by the lens aberrations. Figure 9(b) shows how the amplitude of the function  $a_j$  is affected by defocus. The phase of  $a_j$  changes with position. For the Airy disc in figure 9(a), adjacent rings have a relative phase of  $\pi$  since the amplitude changes sign with every zero crossing. For the defocused probe in figure 9(b), the phase changes are more complicated.

In disordered materials, fluctuations in scattered intensity between sub-volumes show up as a speckle. The speckle is most easily quantified by computing the mean and the variance of the image intensity. The normalized variance of an image is given by

$$V(\mathbf{q}, K_{\text{ap}}) = \frac{\langle I^2(\mathbf{q}, K_{\text{ap}}) \rangle}{\langle I(\mathbf{q}, K_{\text{ap}}) \rangle^2} - 1. \quad (8)$$



As we shall see later, normalization of the second moment of the intensity  $\langle I^2(\mathbf{q}, K_{\text{ap}}) \rangle$  by  $\langle I(\mathbf{q}, K_{\text{ap}}) \rangle^2$  eliminates from  $V(\mathbf{q}, K_{\text{ap}})$  (in principle) the dependence on the scattering form factor  $f(|\mathbf{q}|)$ .

In order to understand how correlations contribute to this speckle, we need to derive expressions for the first and second moments of the image intensity,  $\langle I(\mathbf{q}, K_{\text{ap}}) \rangle$  and  $\langle I^2(\mathbf{q}, K_{\text{ap}}) \rangle$ .

For fixed illumination, the kinematical dark field image wave function is the sum of the individual scattering wave functions,

$$U_j(\mathbf{r}, \mathbf{q}, K_{\text{ap}}) = \sum_j u_j(\mathbf{r}, \mathbf{r}_j, \mathbf{q}, K_{\text{ap}}). \quad (9)$$

The dark field image intensity  $I(\mathbf{r}, \mathbf{q}, K_{\text{ap}})$  is then

$$\begin{aligned} I(\mathbf{r}, \mathbf{q}, K_{\text{ap}}) &= \sum_j \sum_l u_j(\mathbf{r}, \mathbf{r}_j, \mathbf{q}, K_{\text{ap}}) u_l^*(\mathbf{r}, \mathbf{r}_l, \mathbf{q}, K_{\text{ap}}) \\ &= f^2(|\mathbf{q}|) \sum_j \sum_l a_j(\mathbf{r}, \mathbf{r}_j, K_{\text{ap}}) a_l^*(\mathbf{r}, \mathbf{r}_l, K_{\text{ap}}) e^{-i\mathbf{q} \cdot \mathbf{r}_{jl}}, \end{aligned} \quad (10)$$

where  $\mathbf{r}_{jl} = \mathbf{r}_l - \mathbf{r}_j$ , the position vector of scatterer  $l$  relative to scatterer  $j$ . Scatterers  $l$  and  $j$  are assumed to have similar scattering factors.

The mean image intensity  $\langle I(\mathbf{q}, K_{\text{ap}}) \rangle$  is the average intensity over the sample

$$\langle I(\mathbf{q}, K_{\text{ap}}) \rangle = \frac{f^2(|\mathbf{q}|)}{\mathcal{A}} \sum_j \sum_l e^{-i\mathbf{q} \cdot \mathbf{r}_{jl}} \iint_{\text{sample}} a_j a_l^* d^2\mathbf{r}, \quad (11)$$

where  $\mathcal{A}$  is the image area. It can be shown straightforwardly that

$$\iint_{\text{sample}} a_j a_l^* d^2\mathbf{r} = \lambda^2 \iint_{\text{obj}} e^{i\mathbf{k} \cdot \mathbf{r}_{jl}} d^2\mathbf{k}, \quad (12)$$

and we can write for the mean intensity

$$\langle I(\mathbf{q}, K_{\text{ap}}) \rangle = \frac{\lambda^2 f^2(|\mathbf{q}|)}{\mathcal{A}} \sum_j \sum_l \iint_{\text{obj}} e^{i(\mathbf{k}-\mathbf{q}) \cdot \mathbf{r}_{jl}} d^2\mathbf{k}. \quad (13)$$

As before,  $\mathbf{k} - \mathbf{q}$  is the total scattering vector experienced by the beam at  $\mathbf{k}$  in the objective aperture. As expected, the average image intensity is equal to the total diffracted intensity collected by the objective aperture and averaged over the image area. For large enough areas  $\mathcal{A}$ , the average image intensity is independent of the microscope aberration function  $\gamma(|\mathbf{k}|)$ .

From equation (10), the second moment of the image intensity can be written as

$$\langle I^2(\mathbf{q}, K_{\text{ap}}) \rangle = \frac{f^4(|\mathbf{q}|)}{\mathcal{A}} \sum_j \sum_l \sum_m \sum_n e^{-i\mathbf{q} \cdot (\mathbf{r}_{jl} + \mathbf{r}_{mn})} \iint_{\text{sample}} a_j a_l^* a_m a_n^* d^2\mathbf{r}. \quad (14)$$

After some manipulation, the integral over the sample can be reduced to

$$\begin{aligned} \iint_{\text{sample}} a_j a_l^* a_m a_n^* d^2\mathbf{r} &= \lambda^2 \iint_{\text{obj}} d^2\mathbf{k}_1 d^2\mathbf{k}_2 d^2\mathbf{k}_3 e^{i\mathbf{k} \cdot (\mathbf{r}_{jn} + \mathbf{r}_{nl} + \mathbf{r}_{mn})} \\ &\quad \times e^{i(-\gamma(|\mathbf{k}_1|) + \gamma(|\mathbf{k}_2|) - \gamma(|\mathbf{k}_3|) + \gamma(|\mathbf{k}_1 - \mathbf{k}_2 + \mathbf{k}_3|))}. \end{aligned} \quad (15)$$

Considerable simplification can be achieved if we assume that the aberration terms  $\gamma(|\mathbf{k}|)$  are all zero. This is justifiable for most FEM studies, since we are operating far from the resolution limit of the instrument. Small apertures are chosen in order to generate broadened point-spread functions with resolutions near 1.5 nm, compared with  $\leq 0.2$  nm

nominal resolution for most modern TEMs. The aberration terms are not the limiting factor when operating close to focus and can usually be ignored. However, studies involving focal series will need to consider the aberration terms. For images that are in focus, the second moment is well approximated by

$$\langle I^2(\mathbf{q}, K_{\text{ap}}) \rangle = \frac{\lambda^4 f^4(|\mathbf{q}|)}{\mathcal{A}} \sum_j \sum_l \sum_m \sum_n e^{-i(\mathbf{q} \cdot \mathbf{r}_{jl} + \mathbf{q} \cdot \mathbf{r}_{mn})} \times \int_{\text{obj}} e^{i\mathbf{k}_1 \cdot \mathbf{r}_{jn}} d^2 \mathbf{k}_1 \int_{\text{obj}} e^{i\mathbf{k}_2 \cdot \mathbf{r}_{nl}} d^2 \mathbf{k}_2 \int_{\text{obj}} e^{i\mathbf{k}_3 \cdot \mathbf{r}_{mn}} d^2 \mathbf{k}_3. \quad (16)$$

Two distinct types of interference terms are appearing in both the first and second moments of the intensity,

$$F_{jl} = e^{-i\mathbf{q} \cdot \mathbf{r}_{jl}} \quad (17)$$

and

$$A_{jl} = \int_{\text{obj}} e^{i\mathbf{k} \cdot \mathbf{r}_{jl}} d^2 \mathbf{k} = \frac{2J_1(K_{\text{ap}}|\mathbf{r}_{jl}|)}{K_{\text{ap}}|\mathbf{r}_{jl}|}. \quad (18)$$

$2J_1$  is the first-order Bessel function. The  $F_{jl}$  terms represent the coherence strength for interference between scatterers  $j$  and  $l$ . For the plane wave illumination that we have considered up to now, this is a simple sinusoidal interference function. The  $A_{jl}$  are equivalent to  $-ia_{jl}/\lambda$  and are thus proportional to the value of the point-spread function (or probe function)  $a_j$  at position  $\mathbf{r} = \mathbf{r}_l$ . These functions have the Hermitian property  $F_{jl} = F_{lj}^*$  and  $A_{jl} = A_{lj}^*$ . The  $F_{jl}$  interferences are controlled by the illumination optics, and the  $A_{jl}$  interferences are controlled by the imaging optics.

Using this notation, the expressions for the first and second moments of the image intensity become

$$\langle I(\mathbf{q}, K_{\text{ap}}) \rangle = \frac{\lambda^2 f^2(|\mathbf{q}|)}{\mathcal{A}} \sum_j \sum_l A_{jl} F_{jl} \quad (19)$$

and

$$\langle I^2(\mathbf{q}, K_{\text{ap}}) \rangle = \frac{\lambda^4 f^4(|\mathbf{q}|)}{\mathcal{A}} \sum_j \sum_l \sum_m \sum_n A_{jn} A_{nl} A_{mn} F_{jl} F_{mn}. \quad (20)$$

The normalized variance of equation (8) can now be written compactly as

$$V(\mathbf{q}, K_{\text{ap}}) = N_0 \frac{\sum_j \sum_l \sum_m \sum_n A_{jn} A_{nl} A_{mn} F_{jl} F_{mn}}{\sum_p \sum_q \sum_r \sum_s A_{pq} A_{rs} F_{pq} F_{rs}} - 1 \equiv \frac{\sum_{j,l,m,n} (N_0 A_{jn} A_{nl} - A_{jl}) A_{mn} F_{jl} F_{mn}}{\sum_{p,q,r,s} A_{pq} A_{rs} F_{pq} F_{rs}}. \quad (21)$$

$N_0 = \mathcal{A} \pi K_{\text{ap}}^2$  is the image area  $\mathcal{A}$  divided by the characteristic area of the resolution function  $\pi K_{\text{ap}}^2$  and is thus equivalent to the number of pixel elements in the image.

The normalized variance  $V(\mathbf{q}, K_{\text{ap}})$  depends on 4-body, or pair-pair, correlations. Whereas the mean diffracted intensity depends on 2-body, or pair, correlations. This dependence on higher order correlations bestows  $V(\mathbf{q}, K_{\text{ap}})$  with increased sensitivity to medium range order compared with the mean diffracted intensity  $\langle I(\mathbf{q}, K_{\text{ap}}) \rangle$ .

In the TEM, the properties of the illumination coherence function  $F_{jl}$  can be modified by changing the properties of the illumination, such as the convergence. Incoherent hollow cone illumination can be generated by spinning the tilted illumination vector  $\mathbf{q}$  azimuthally

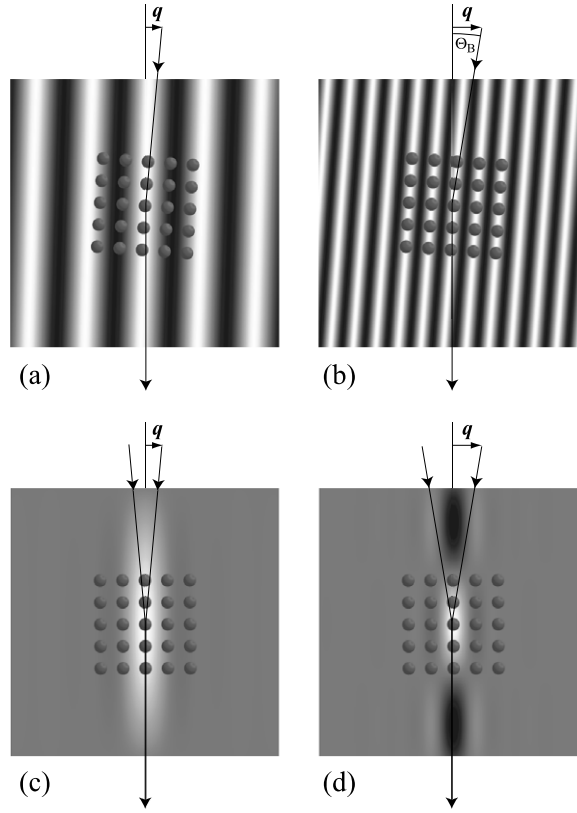


**Figure 10.** Grey-scale representations of the coherence function  $F_{jl}$  for various illumination conditions. The spheres represent a crystalline array of scatterers. The illumination is incident from the top. The vertical direction represents depth  $z$  through the sample thickness. Bright regions indicate positive amplitude and represent those regions where scattering from some scatterer  $j$  will be in phase with scattering from the central scatterer  $l$  for constructive interference. The dark regions indicate negative amplitude, where destructive interference occurs. (a) Low angle tilted plane wave illumination. The coherence function has a widely spaced periodicity. (b) Plane wave illumination tilted at the Bragg angle  $\theta_B$ . The scattering from all atoms interferes constructively. (c) Low angle incoherent hollow cone illumination. Constructive interference is strongest for atoms  $j$  that are in the same column as the central atom  $l$ . (d) High angle incoherent hollow cone illumination. Alternating zones of constructive and destructive interference appear along the columns.

(see figure 7(a)). Images are built up as an incoherent sum over the azimuthal angles. The  $F_{jl}$  terms are then modified to [26]

$$F_{jl} = \frac{\int_{\alpha_1}^{\alpha_2} J_0(2\pi\sigma_{jl}\sin(\alpha)/\lambda) \cos(4\pi z_{jl}\sin^2(\alpha/2)/\lambda) f(\alpha)^2 \alpha d\alpha}{\int_{\alpha_1}^{\alpha_2} f(\alpha)^2 \alpha d\alpha}. \quad (22)$$

$J_0$  is the zero-order Bessel function.

Here we have decomposed the atom position into an in-plane  $x$ - $y$  component  $\sigma_{jl}$  and the  $z$ -component  $z_{jl}$ , thus  $\mathbf{r}_{jl} \equiv (\sigma_{jl}, z_{jl})$  and have used the cone tilt angle  $\alpha = \sin^{-1}(\lambda|\mathbf{q}|/2\pi)$ . The hollow cone illumination serves to suppress the lateral extent of the coherence function, increasing the relative importance of interferences between atoms that line up in columns [28, 29].

Figure 10 compares the coherence functions for plane wave illumination (figures 10(a) and (b)) and for hollow cone illumination (figures 10(c) and (d)) at two tilt angles. Superimposed

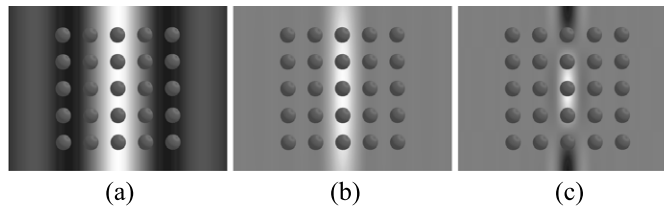


**Figure 11.** Grey-scale representations of the resolution function  $A_{jl}$  for various illumination conditions. The spheres represent a crystalline array of scatterers. The illumination is incident from the top. The vertical direction represents depth  $z$  through the sample thickness. Bright regions indicate positive amplitude and represent those regions where scattering from some scatterer  $j$  will be in phase with scattering from the central scatterer  $l$  for constructive interference. The dark regions indicate negative amplitude, where destructive interference occurs. (a) Airy disc (side view). (b) Combined effect of the resolution function  $A_{jl}$  and the coherence strength  $F_{jl}$  for low angle hollow-cone, (c) combined effect for a higher angle hollow-cone.

on these functions is a hypothetical lattice of atoms in an ordered square array. In figure 10(b), the lattice and the coherence function are resonant, with every atom aligned on a peak of the coherence function. This is the Bragg reflection condition for this lattice. The hollow cone coherence function suppresses the lateral periodic ripples, so that most of the interference arises between scatterers that are aligned in columns (figures 10(c) and (d)). In practice, the normalized variance in hollow cone illumination is significantly suppressed relative to the variance for tilted dark field at the same tilt angle.

Figure 11(a) shows a side view of the resolution function  $A_{jl}$ . As in figure 10, the vertical axis represents height  $z$  within the sample. The central vertical white band represents the side view of the central disc of the Airy function projected through the sample. In this simple schematic, the depth of focus is assumed to be infinite, so the function depicted here is assumed to not vary significantly with depth. Superposed is a hypothetical lattice of atoms. The resolution function depicted here is not narrow enough to resolve the lattice, having a width corresponding to about 2 lattice spacings. Figures 11(b) and (c) show the combined effect of the Airy function of figure 11(a) and the hollow cone coherence strengths depicted in figures 10(c) and (d). The region around each scatterer  $l$  within which coherent scattering with  $j$  can occur is controlled by the intersection of both the  $F_{jl}$  and the  $A_{jl}$  functions. These functions can be independently controlled. Experiments where  $F_{jl}$  is varied are sometimes referred to as variable coherence fluctuation microscopy, and experiments where the  $A_{jl}$  is varied are referred to as variable resolution microscopy.

As equation (21) reveals, the speckliness of a dark field image, as measured by the normalized variance, is dependent on 4-body correlations. The mean image intensity is a measure of the average diffracted intensity collected by an objective aperture and is dependent only on the 2-body terms. Thus, the normalized variance depends on higher order correlation functions. This dependence on higher order correlations up to 4-body terms is what gives fluctuation microscopy its sensitivity to medium range order.

Figure 12 shows a simplified physical picture of how fine-scale image speckle reveals medium range order in amorphous silicon. On the left, the sample is a CRN (represented as localized  $\sim 1$  nm regions extracted from the matrix) with no local crystalline order. On the right, the sample is ordered, comprising  $\sim 1$  nm regions (paracrystallites) that have the cubic Si structure. Speckle from the CRN sample on the left arises from random atom alignments that generate coherent constructive and destructive interference of scattered waves at the statistical level. On the right, speckle is augmented by coherent microdiffraction from the ordered regions.

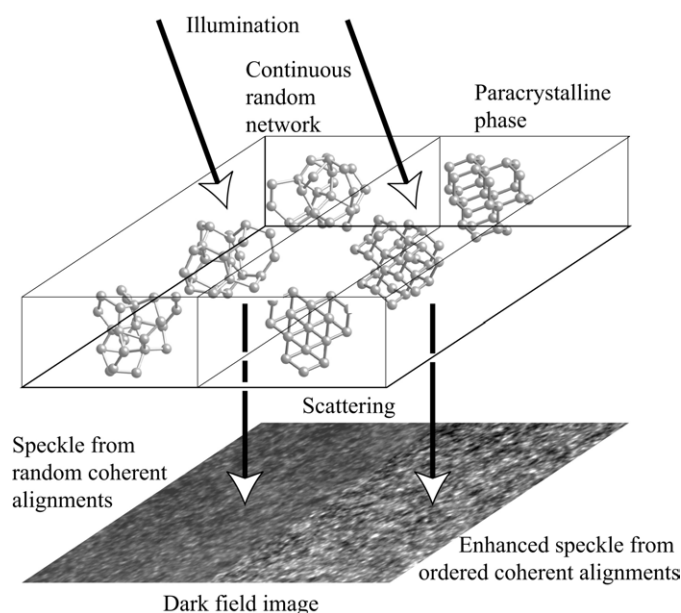


**Figure 12.** A simplified explanation of how fluctuation microscopy works in TEM for the case of tilted illumination. On the left-hand side a dark-field image from a disordered CRN-type of specimen exhibits speckle (image intensity fluctuations) due to random alignments of coherently scattering atoms. On the right-hand side a structure with paracrystalline medium range order will exhibit increased speckle because of random alignments of small locally ordered regions that are near a Bragg diffraction condition. Ordered materials will exhibit peaks in the intensity variance when the scattering conditions favour such Bragg reflections. CRN materials will not exhibit such characteristic peaks.

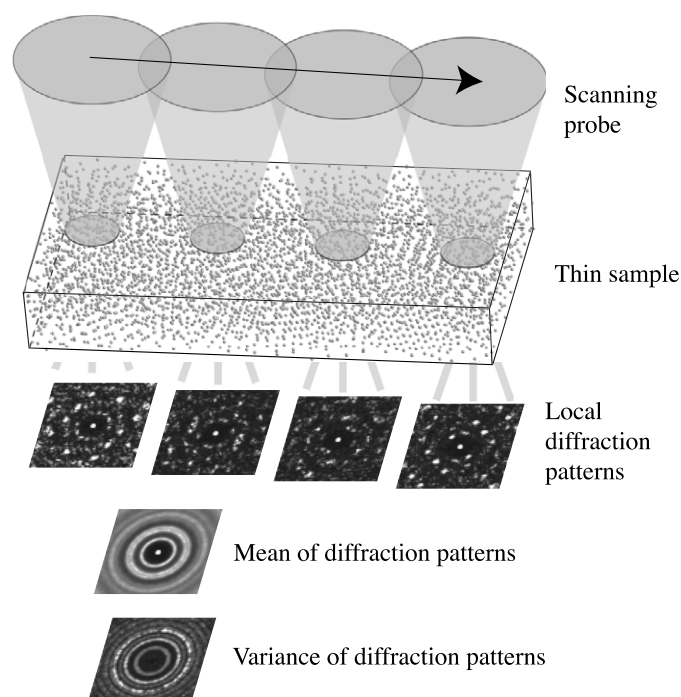
This speckle has a strong diffraction vector ( $q$ ) dependence and is revealed by examining the speckle as a function of  $q$ .

Figure 12 presents the TEM viewpoint of fluctuation microscopy, where the diffraction vector  $q$  is fixed and the data are collected as dark-field images with intensity varying with position  $r$ , i.e. data are collected as  $I(q_{\text{fixed}}, r)$ . An alternative, but essentially equivalent, view of fluctuation microscopy is from the STEM viewpoint, where the sample is probed one small volume at a time, and it is the diffraction patterns that are collected, i.e. data are collected as  $I(q, r_{\text{fixed}})$ . This experimental scheme is depicted in figure 13. In this mode, it is the speckle statistics in diffraction patterns that are collected. In principle, if the TEM mode scans all  $q$  and the STEM mode scans all  $r$ , the two data sets will be identical.

The mean image intensity is readily inverted to give a radial distribution function or RDF. The smaller the objective aperture gets, the better the  $q$ -resolution of the diffraction data becomes. As shown by McBride and Cockayne [61, 62], localized pair distribution functions can be obtained by microdiffraction from small volumes. Such nano-RDF techniques offer a powerful complementary method for examining the local structure of nanosized disordered regions, such as in cross-section images of dielectric layers in electronic devices.

## 2.2. Models of disorder and medium range order

At the time of writing, fluctuation microscopy data cannot be readily inverted or refined to provide a model of the disordered structure. Instead, a pragmatic approach has been to compare



**Figure 13.** Diagram depicting the STEM scattering geometry for fluctuation microscopy. The focused probe is scanned over the sample. Diffraction patterns at each point are collected. The mean and variance of the diffraction patterns over all sample points are computed. Rotationally averaged traces through the variance maps are equivalent to the incoherent hollow-cone variance plots, such as shown in figure 6.

data with simulations from models. Consequently, conclusions about the samples tend to be only as good as the best models. Thus, realistic models are important.

Since most of our fluctuation microscopy data to date have been FEM studies of amorphous Si and Ge, we shall focus our discussion here on those amorphous tetrahedral semiconductors. As is outlined in the introduction, there is also significant literature on metallic glasses, oxide glasses as well as sphere packings, but we do not discuss those here.

Although Zachariasen introduced the concept of a CRN for tetrahedral frameworks in 1932 [11], it was not until the early 1970s that actual CRN models, with atomic coordinates, became available. Polk and co-workers built their early CRN models by hand [66, 67], including models that contained vacancies [68]. Wooten *et al* [69, 70] established a more reliable bond breaking/making computer algorithm that generated larger disordered models with strict 4-coordination and maintaining low strain energy. Similarly, Biswas generated models specific to Ge [71–73]. These CRN models for Si and Ge were used in the early FEM work [32, 33]. However, these models contained no significant amounts of medium range order and could not duplicate the experimental FEM data.

Keblinski and colleagues [74–77] created a series of metastable models by imbedding randomly oriented nanocrystals of cubic Si into a CRN matrix and allowing the system to relax by molecular dynamics methods. This generated a series of models that qualitatively matched the characteristics of the experimental FEM data. Figure 14 shows  $\sim 2$  nm diameter fragments from two models. Figure 14(a) shows a fragment from the 4096-atom model of Wooten *et al* [69, 70], which we here refer to as W2. No apparent ordering is visible.

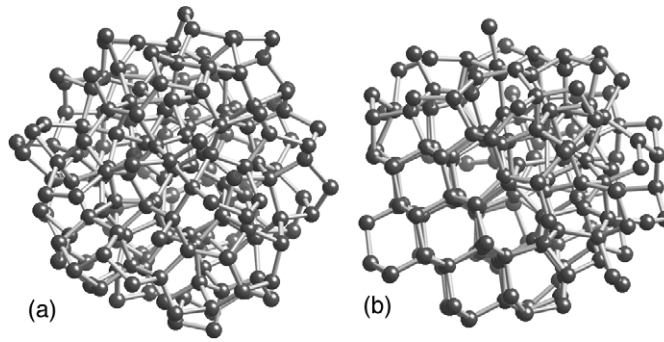


**Figure 14.** Fragments from two models of disorder. (a) CRN model W2 containing 4096 atoms in a periodically repeating cell due to Wooten *et al* [69,70]. (b) Paracrystallite model K3 containing 1024 periodic atoms due to Koblinski *et al* [74–77]. The paracrystallite evident in (b) is heavily strained.

Figure 14(b) shows a fragment from a 1024-atom model of Koblinski, K3. Here, an ordered fragment is visible. Clearly the fragment has the cubic diamond bonding, but the fragment is strained. These nanoscale fragments are referred to as *paracrystallites*. A paracrystal is an organized assembly of atoms, which locally appear to lie on a crystalline lattice, but deviate increasingly from that lattice as the inter-atomic distances increase [78,79]. A crystal with strong shear strain *gradients* would be paracrystalline. The models of Koblinski *et al* [74–77] represented a compact of paracrystallites with disordered Si at the interfaces. The strong shear strain gradients in the paracrystals are what distinguish them from a polycrystalline compact.

Recent work using ECMR methods [80,81], where experimental FEM data is the target fitting function, has generated intriguing alternative models that reproduce some of the essential FEM data for amorphous Si but do not contain paracrystallites. These results highlight the non-uniqueness of solutions to the inversion problem. It is clear that sophisticated fitting procedures such as ECMR, in conjunction with good physical judgment, will probably offer the most reliable methods for interpreting structures from FEM data.

### 2.3. Computational models

Given a model of a disordered material, a direct application of equation (21) to compute the variance can present severe computational difficulties. For a model containing  $N$  scatterers, the 4-body summation in the numerator will contain  $N^4$  terms. The denominator, representing the square of the mean intensity, contains  $N^2$  terms. Strategies that avoid double counting of interference terms, by exploiting the Hermitian properties of  $F_{jl}$  and  $A_{jl}$ , do not gain much more than a factor of two in speed. Consequently, as written, equation (21) is not practical for simulations of large models containing more than about 500 atoms. Another computational strategy is to exploit the columnar form of the  $A_{jl}$  and  $F_{jl}$  functions and to restrict computational effort only to those atoms  $j$  that have small values of  $\sigma_{jl}$ .

Figure 15 shows simulations of  $V(\mathbf{q}, K_{\text{ap}})$  for two models of disordered germanium. Model W1 contains 216 atoms, and is due to Wooten *et al* [69,70], and the second model K1, containing 512 atoms, is due to Koblinski *et al* [74–77]. Both models were originally computed for Si, but were rescaled for Ge–Ge bonds distances. Both simulations were made by an explicit computation of the 4-body expression in equation (21). It was found that the 512-atom model is close to the practical upper limit for brute-force computations of this kind. It was assumed



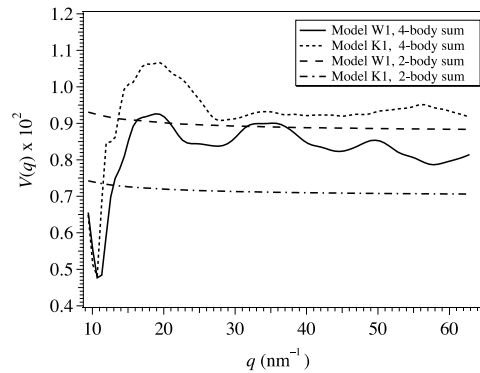


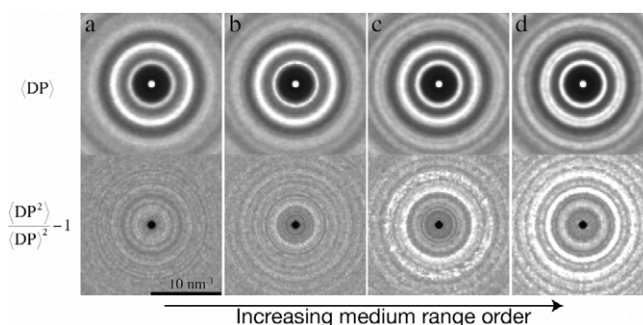
**Figure 15.** Simulations of  $V(q)$  for two models of amorphous silicon. W1 is a 216-atom model due to Wooten *et al* [69, 70]. K1 is a 512-atom paracrystalline model due to Keblinski *et al* [74–77]. When using the full 4-body summation, both models produce the experimentally observed features at  $q = 19$  and  $35 \text{ nm}^{-1}$ , but with reduced amplitude. The 2-body summations (averaged diffraction) do not reproduce the peaks.

that the resolution functions were perfect Airy disc type functions, with  $K_{\text{ap}} = 9.4 \text{ nm}^{-1}$ . The  $F_{ji}$  functions were modelled for a narrow hollow cone illumination with cone semi-angle  $q/\chi$ . Both models exhibit peaks near  $q = 19$  and  $35 \text{ nm}^{-1}$ , in similar locations to those observed in the experimental data of figure 6, but with different peak heights.

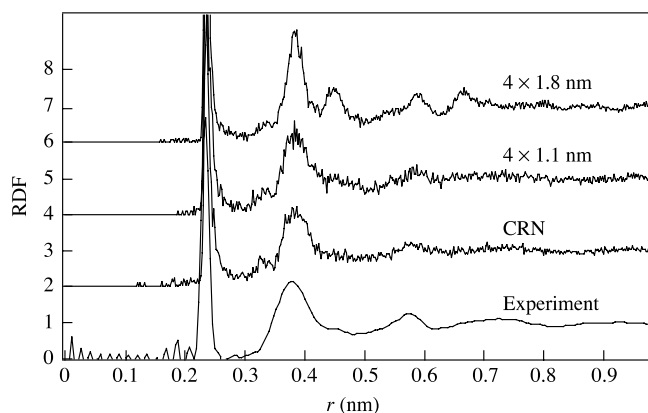
A more efficient method for computing the variance from models is to simulate images or diffraction patterns for many different orientations and regions of the model. Both the image and diffraction pattern can be computed as 2-body summations over the model's atom locations, such as in equation (10) or even by using multi-slice methods [33, 34]. Computing an image or diffraction pattern for a given position and orientation requires a computational effort of the order of  $N^2$  when there are  $N$  atoms in the model [82–84], as opposed to the prohibitive  $N^4$  demanded by equation (21).

Figure 16 shows the mean diffraction patterns (top row) and the variance patterns, or fluctuation patterns (bottom row), for four models K1, K2, K3 and K4 due to Keblinski *et al* [74–77]. The patterns are the averages and variances of 1000 randomly-oriented simulated kinematical microdiffraction patterns taken from a thickness of  $\sim 2 \text{ nm}$ , using a Gaussian probe profile of standard deviation  $0.75 \text{ nm}$  (nominal point-spread function of  $1.5 \text{ nm}$  diameter). The diffraction plots have been normalized for the atomic form factor of Si, which ordinarily causes a fall in intensity with increasing scattering vector. These simulations are equivalent to a STEM experiment, where the sample is probed point by point, recording the diffraction pattern at each point. A radial scan through the variance plots is equivalent to a simulation of  $V(q, K_{\text{ap}})$  versus  $q$  plot, such as in figure 15. The CRN model K1, figure 16(a), has a weak variance signal, revealing insignificant medium range order. For the paracrystalline model K2, figure 16(b), with grain diameter of  $1.1 \text{ nm}$ , the diffraction pattern is almost identical to that for the CRN, but the fluctuation pattern reveals a significant increase in signal near the cubic 111 diffraction ring. The fluctuation patterns for the paracrystalline models with typical grain diameters of  $1.5 \text{ nm}$  and  $1.8 \text{ nm}$ , in figures 16(c) and (d), show increasingly stronger variance features. It is only for the mean diffraction pattern of model K4 in figures 16(d) that subtle departures from the CRN model appear. The mean diffraction patterns for models K1, K2 and K3 are similar, whereas the fluctuation patterns show more clearly the evolution of medium range order. As an aside, there will be a small contribution to the computed variance in figure 16 due to statistical fluctuations in the number of atoms





**Figure 16.** Computed mean diffraction patterns (upper row), and associated fluctuation patterns (lower row), for four models of disordered Si possessing increasing amounts of medium range order. The upper patterns are the averages of 1000 randomly-oriented microdiffraction patterns taken from a thickness of 2 nm, using a Gaussian probe of standard deviation 0.75 nm (nominal point spread function of 1.5 nm diameter). These plots have been normalized for the atomic form factor of Si, which ordinarily causes a fall in intensity with increasing scattering vector, and are sensitive to the details of the second-order (pair) atomic correlations. The lower patterns are the normalized variances of the 1000 diffraction patterns—the fluctuation patterns—and these are sensitive to fourth-order (pair-pair) atomic correlations [61]. (a) CRN. The variance signal is weak, revealing insignificant medium range order. (b) Paracrystalline model with grain diameter of 1.1 nm. The diffraction pattern is almost identical to that for the CRN, but the fluctuation pattern reveals a significant increase in medium range order. (c) Paracrystalline model with typical grain diameter of 1.5 nm. (d) Paracrystalline model with typical grain diameter of 1.8 nm. Subtle features appear in the latter two diffraction patterns, but strong signatures of medium range order are clear in the fluctuation patterns.



**Figure 17.** RDFs for three models of amorphous Si containing different extents of medium range order, compared with experimental data for an amorphous Si sample. Models for a CRN and for  $\sim 1.1$  nm diameter paracrystallites are essentially indistinguishable from each other and from experimental data. The model for  $\sim 1.8$  nm paracrystallites is more readily distinguished from the CRN.

included in each randomly-oriented simulation. However, these fluctuations are not expected to produce peaks.

The RDFs for K1, K2 and K3 were computed (by real-space averaging methods) and are compared in figure 17 with experimental data for amorphous Si. The data for model K3 (1.8 nm diameter paracrystallites) are readily distinguishable from the experimental data, but models K1 and K2 are similar.

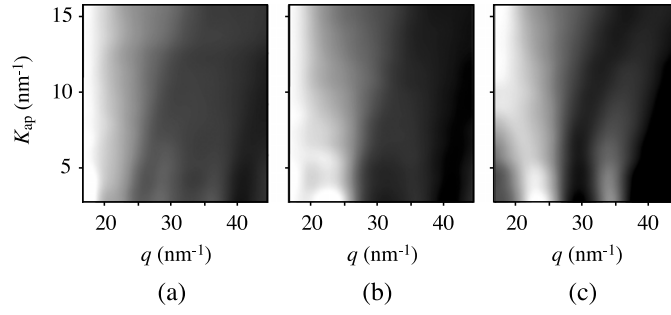


**Figure 18.** Simulated fluctuation maps for three models of amorphous Si, where the normalized variance  $V(\mathbf{q}, K_{\text{ap}})$  is plotted as an intensity value as a function of  $K_{\text{ap}}$  (vertical axis) and  $\mathbf{q}$  (horizontal axes). (a) CRN. (b)  $\sim 1.1$  nm paracrystallite model. (c)  $\sim 1.8$  nm paracrystallite model. Plots (b) and (c) exhibit the two broad vertical bands, which correspond to the two characteristic peaks that appear in  $V(\mathbf{q}, K_{\text{ap}})$  versus  $\mathbf{q}$  plots.

Figures 18(a)–(c) show simulated fluctuation maps for three models of amorphous Si, K1, K2 and K4, where the normalized variance  $V(\mathbf{q}, K_{\text{ap}})$  is plotted as an intensity value as a function of the objective aperture  $K_{\text{ap}}$  (vertical axis) and the hollow cone  $\mathbf{q}$  (horizontal axis). Plots 18(b) and (c) exhibit two broad vertical bands, which correspond to the two characteristic peaks that appear in  $V(\mathbf{q}, K_{\text{ap}})$  versus  $\mathbf{q}$  plots (which are equivalent to horizontal traces through these plots). For values of  $K_{\text{ap}} \leq 15 \text{ nm}^{-1}$ , the intensity appears as vertical striations. This observation provides some validation for models that separate the  $\mathbf{q}$  and  $K_{\text{ap}}$  dependences of  $V(\mathbf{q}, K_{\text{ap}})$  into two independent functions, as will be discussed later.

Earlier models of speckle were more phenomenological, approaching the issue from a statistical viewpoint. One of the simplest models of TEM dark-field speckle assumes that the coherent scattering is from a random assembly of atoms [20, 21]. Suppose the wave scattered at any given pixel is  $a + ib$ , where  $a$  and  $b$  are independently Gaussian-distributed with the same standard deviation  $\sigma$  such that

$$P(a, b) da db = \frac{1}{2\pi\sigma^2} \exp\left(-\frac{a^2 + b^2}{2\sigma^2}\right) da db. \quad (23)$$

If we rewrite  $a + ib = c \exp(i\phi)$ , then the local image intensity is  $I = c^2 = a^2 + b^2$  and we have  $P(a, b) da db \equiv P(c, \phi) c dc d\phi \equiv \frac{1}{2} P(I, \phi) dI d\phi$ . The image intensity distribution can then be expressed as

$$P(I) dI = \frac{1}{2\pi\sigma^2} \int_{-\pi}^{\pi} c \exp\left(-\frac{c^2}{2\sigma^2}\right) dc d\phi = \frac{1}{\langle I \rangle} \exp\left(-\frac{I}{\langle I \rangle}\right) dI, \quad (24)$$

giving a mean intensity  $\langle I \rangle = 2\sigma^2$ . The second moment of this distribution equals  $\langle I^2 \rangle = 2\langle I \rangle^2$  giving a normalized variance  $V = 1$ , independent of either  $\mathbf{q}$  or  $K_{\text{ap}}$ . However, experimental tilted dark field images of amorphous materials invariably have much lower values for the normalized variance,  $V \ll 1.0$ . For example, the tilted dark-field image in figure 4, of a 23 nm thick Ge film, has  $V \approx 0.1$ . Incoherent hollow cone dark-field images have significantly lower normalized variance,  $V \approx 0.01$ . Clearly, illumination coherence has an important influence on speckle variance.

A refinement of the above model introduces a phenomenological correction for partial coherence of the illumination. Assuming that there are  $m$  independent partial illumination sources irradiating the specimen, an analysis similar to that described above, including

averaging over the sources, leads to the gamma distribution [21]

$$P(I) = \frac{m^m}{(m-1)!} \frac{I^{m-1}}{\bar{I}^m} \exp\left(-\frac{mI}{\bar{I}}\right). \quad (25)$$

With  $m = 1$ , equation (25) is equivalent to equation (24). The second moment is related to the first moment through

$$\langle I^2 \rangle = \frac{m+1}{m} \langle I \rangle^2, \quad (26)$$

and the normalized variance is then simply  $V = 1/m$ . As  $m \rightarrow \infty$ ,  $V \rightarrow 0$ , which is equivalent to superimposing a large number of uncorrelated speckle images. The normalized variance measured for figure 4 implies  $m \approx 10$  suggesting that figure 4 is equivalent to the incoherent superposition of about 10 coherent dark-field images. Despite its apparent simplicity, the gamma distribution (equation (25)) is difficult to understand in experimental terms. What is the meaning of  $m$  as an independent variable? Is it controlled entirely by the illumination or is it partly governed by non-kinematical contributions to the scattering, such as inelastic scattering? Such questions could be addressed effectively in more modern TEM instruments that allow images to be energy-filtered. In addition, how does the non-random short-range order affect the analysis?

Furthermore, in the incoherent limit where  $m \rightarrow \infty$ , the gamma distribution fails to take into account the statistics of the atom distribution in thin disordered specimens.

To address this limitation, Treacy and Gibson [85] decomposed the 4-body terms in equation (21) into 15 distinct domains, within each of which no scatterer is counted twice. These domains are represented by the list of constraints

$$\begin{aligned} j=l=n=m \quad (j=n) \neq (l=m) \quad (j=m) \neq (l=n) \quad (j=l) \neq (m=n) \quad (j=m=n) \neq l \\ (l=m=n) \neq j \quad (j=l=n) \neq m \quad (j=l=m) \neq n \quad (m=n) \neq j \neq l \quad (j=n) \neq l \neq m \\ (l=n) \neq j \neq m \quad (j=m) \neq l \neq n \quad (l=m) \neq j \neq n \quad (j=l) \neq m \neq n \quad j \neq l \neq m \neq n. \end{aligned}$$

These include one 1-body term, seven 2-body terms, six 3-body terms and one 4-body term. Assuming that there are many scatterers in the sample and that their positions are random, then terms of the type  $F_{jl}$  and  $F_{jl}F_{mn}$  average to zero, whereas terms of the type  $|F_{jl}|^2$  are non-zero. In the limit of uncorrelated atom positions, the normalized variance can be expressed as

$$V(\mathbf{q}) \approx 2\langle F^2(\mathbf{q}) \rangle + \frac{1}{\langle n \rangle} - \frac{1}{N}. \quad (27)$$

Here,  $N$  is the total number of scatterers contributing to the image and  $\langle n \rangle = N/N_0$  is the average number of scatterers per pixel column.  $\langle F^2(\mathbf{q}) \rangle$  represents the average value of  $F_{jl}$  ( $j \neq l$ ). When the positions of the scatterers are fully random,  $\langle F^2(\mathbf{q}) \rangle$  is determined entirely by the illumination geometry.

Under conditions of perfect spatially coherent illumination, we can set  $\langle F^2(\mathbf{q}) \rangle = 0.5$ . With  $N, N_0 \gg 1$  we get

$$V \approx 1 + \frac{1}{\langle n \rangle} - \frac{1}{N}. \quad (28)$$

The  $V = 1$  term dominates and is the result expected for negative exponential statistics (equation (24)) for a sample with  $N \rightarrow \infty$  uncorrelated atoms. The  $1/\langle n \rangle$  term is the Poisson statistics contribution coming from the variation in the number of scatterers per sampled volume i.e. per pixel, and the  $1/N$  term is from the sample statistics. The columnar  $1/\langle n \rangle$  ‘scatterer noise’ term is not considered in the negative exponential or gamma-distribution models, which assume infinite thickness with  $\langle n \rangle$  infinite.

In practice, the illumination is never fully coherent, and  $\langle F^2(\mathbf{q}) \rangle \ll 1$  giving values of  $V \ll 1$ —a result that is consistent with experimental data.

In the limit of perfectly incoherent illumination, such as that obtained by a broad angle hollow cone illumination (or equivalently, a high angle annular detector), we have  $\langle F^2(\mathbf{q}) \rangle \rightarrow 0$ , and then

$$V \approx \frac{1}{\langle n \rangle} - \frac{1}{N}, \quad (29)$$

which is simply a measure of the statistics of the projected atom images, with no  $\mathbf{q}$  dependence. Shot noise from the illumination statistics is not included here, but will contribute a  $1/\langle N_{\text{inc}} \rangle$  term, where  $\langle N_{\text{inc}} \rangle$  is the average number of image electrons or photons incident at each pixel.

Although these expressions do a better job of accounting for some of the observed details of experimentally measured variances of dark-field speckle images of amorphous materials, they do not satisfactorily account for the observed  $\mathbf{q}$ -dependence of the variance data. For samples with any short- or medium-range order present, equation (27) is inadequate since it is at best a 2-body approximation, and the full 4-body expression, equation (21), must be used.

Efforts have been made to reduce the second moment of image intensity or the variance into a set of  $n$ -body correlation functions ( $1 \leq n \leq 4$ ). Iwai *et al* showed that the 4-body variance expression could be decomposed into higher-order cumulant functions [86]. Although this appears to be an efficient mathematical approach, their methods have not been implemented experimentally. Gibson *et al* [59] presented integral expressions for  $V(\mathbf{q}, K_{\text{ap}})$  in terms of correlation functions  $g_2(|\mathbf{r}_{jl}|)$ ,  $g_3(|\mathbf{r}_{jn}, \mathbf{r}_{nl}|)$  and  $g_4(|\mathbf{r}_{jn}, \mathbf{r}_{nl}, \mathbf{r}_{mn}|)$ . However, in their general form, their pair-persistence functions  $g_3$  and  $g_4$  appear to be too cumbersome to be useful for experimental analysis. However, by making the approximation that correlations in scattering between scatterers decay on average as a Gaussian function of separation,  $\exp(-|\mathbf{r}_{jl}|^2/2\Lambda^2)$ , with a correlation length  $\Lambda$ , Gibson *et al* [59] argued that under low-resolution conditions the  $\mathbf{q}$  and  $K_{\text{ap}}$  dependences of  $V(\mathbf{q}, K_{\text{ap}})$  could be separated. They showed that the correlation length could be extracted by measuring the normalized variance as a function of the objective aperture size  $K_{\text{ap}}$ . At low resolutions (i.e.  $\geq 0.5$  nm), the  $\mathbf{q}$  and  $K_{\text{ap}}$  dependences could be separated into the form

$$V(\mathbf{q}, K_{\text{ap}}) = P(\mathbf{q}) \left[ \frac{K_{\text{ap}}^2 \Lambda^3}{1 + 4\pi^2 K_{\text{ap}}^2 \Lambda^2} \right], \quad (30)$$

which can be linearized as

$$\frac{1}{V(\mathbf{q}, K_{\text{ap}})} = \frac{4\pi^2}{P(\mathbf{q})\Lambda} + \frac{1}{P(\mathbf{q})\Lambda^3} \frac{1}{K_{\text{ap}}^2}. \quad (31)$$

This equation predicts that plots of  $1/V(\mathbf{q}, K_{\text{ap}})$  versus  $K_{\text{ap}}^{-2}$  should be linear, with a slope  $m$ ,

$$m = \frac{1}{P(\mathbf{q})\Lambda^3} \quad (32)$$

and intercept  $c$ ,

$$c = \frac{4\pi^2}{P(\mathbf{q})\Lambda}, \quad (33)$$

so that the correlation length is

$$\Lambda = \frac{1}{2\pi} \sqrt{\frac{c}{m}}. \quad (34)$$

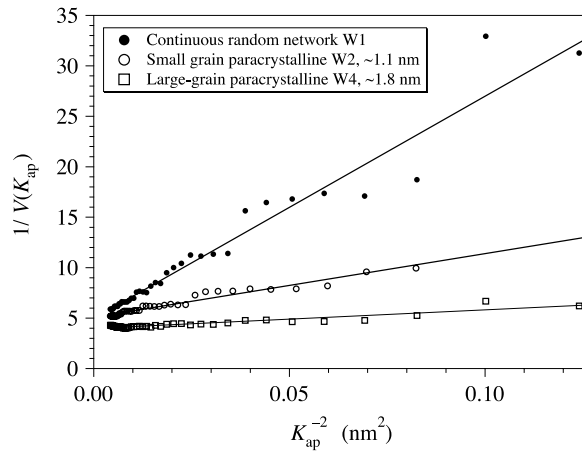


**Figure 19.** Plots of  $1/V(q, K_{ap})$  versus  $1/K_{ap}^2$ , with  $q$  held constant at the first peak  $q = 19 \text{ nm}^{-1}$ , for three models of disordered Si by Kéblinski: the 1024-atom CRN model K3, the 512-atom  $\sim 1.1 \text{ nm}$  paracrystalline model K1 and the 1024-atom  $\sim 1.8 \text{ nm}$  paracrystalline model K4.

The essentially vertical striations in simulations (see figure 18) confirm that at the low resolution limit (small  $K_{ap}$ ), the  $q$  and  $K_{ap}$  dependences of  $V(q, K_{ap})$  are largely decoupled. Values for the correlation length  $\Lambda$ , obtained from speckle simulations of models (figure 19), are  $\Lambda_{K1} = 0.15 \text{ nm}$  for the CRN model K1,  $\Lambda_{K2} = 0.29 \text{ nm}$  for the paracrystallite model K2 and  $\Lambda_{K4} = 0.48 \text{ nm}$  for the paracrystallite model K4. Interpreting  $\Lambda$  as a radius of gyration for the correlated spheroidal regions, we can extract widths  $W$  from the relation  $\Lambda^2 = W^2/10$ . We then get the effective widths,  $W_{K1} = 0.48 \text{ nm}$ ,  $W_{K2} = 0.92 \text{ nm}$  and  $W_{K4} = 1.5 \text{ nm}$ . The values obtained for K2 and K4 are consistent with the mean diameters of paracrystallites present in the models,  $D_{K2} = 1.1 \text{ nm}$  and  $D_{K4} = 1.8 \text{ nm}$ . Interestingly, for the paracrystallite models K2 and K4, the ratio  $D/W = 1.2$ . This may be because the radius of gyration is underestimated when the region is assumed to be spheroidal. There are no topologically paracrystalline regions in model K1. It is likely that the value  $W_{K1} = 0.48 \text{ nm}$  relates to short range order that may be present in the model, even though there are no topologically paracrystalline regions.

#### 2.4. Experimental artefacts

Coherent image speckle is not the only contribution to the variance of the image intensity. Clearly, all physical contributions to the image intensity potentially contribute to the measured variance. The most common sources unrelated to medium range order are: sample thickness changes, illumination intensity gradients across the image, extraneous signals from defective CCD pixels or stray high energy x-rays (in TEM experiments), flicker in the illumination, inconsistencies in operation of beam shutters and shot noise.

Some of these sources can be suppressed by applying appropriate high and low bandpass filters to the data and by normalizing signals to the incident illumination. Shot noise, and CCD detector offsets, can make significant contributions to the normalized variance. It is a routine procedure in most TEM laboratories using CCD cameras to not only normalize images according to a ‘white field’ calibration of the detector response (so-called gain normalization) but also to subtract a detector dark-current signal (i.e. a ‘black field’ exposure with identical collection time as the image, but with no signal). However, for lengthy experimental runs, bypassing the dark-current images can halve the experimental run time. In those cases,

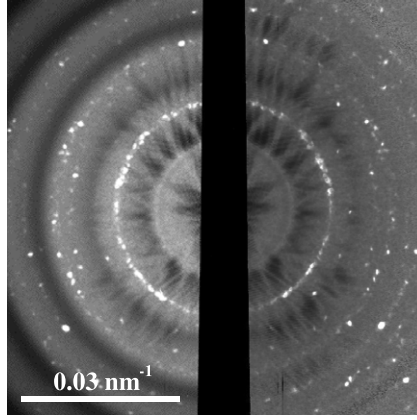


**Figure 20.** X-ray diffraction normalized variance data from a thin ( $\sim 20 \mu\text{m}$ ) film of 277 nm diameter latex spheres using a  $5.5 \mu\text{m}$  probe generated by a pinhole. The dark central band is the beam stop, which blocks the zero-order beam. The left half of the image shows the normalized variance before correction for shot noise. The broad circular bands arise mainly from the shot noise on the form factor for scattering from spherical particles. The right half shows the data corrected for the shot noise using equation (35).

dark-current images collected at the beginning and end of the runs can provide reasonable estimates. The variance of the shot noise is proportional to the number of detected electrons (or x-rays) in each pixel, or simply  $I(\mathbf{q}, K_{\text{ap}})/g$ , where  $g$  is the detector quantum efficiency (i.e. the number of detector electrons per incident electron or x-ray). A simple and effective method for correcting the normalized variance for shot noise is to modify the variance equation (8) to

$$V(\mathbf{q}, K_{\text{ap}}) = \frac{\langle I^2(\mathbf{q}, K_{\text{ap}}) \rangle}{\langle I(\mathbf{q}, K_{\text{ap}}) \rangle^2} - \frac{g}{\langle I(\mathbf{q}, K_{\text{ap}}) \rangle} - 1. \quad (35)$$

It is important that dc offsets in the camera be corrected in the image intensities before computing the normalized variance. Figure 20 shows the normalized variance of the x-ray diffraction pattern from an assembly of 277 nm latex spheres. The left side shows the variance before correction for shot noise; the right side shows the variance after correction for shot noise. The broad rings in the uncorrected data (left) correspond to the shot noise contribution in the spherical scattering form factor. The FXM analysis of this sample is discussed in more detail in section 4.2 later.

An important assumption in our analysis is that the scattering can be treated kinematically—that is, multiple scattering can be ignored. This is a reasonable assumption when the sample thickness is significantly thinner than the mean scattering length. Incoherent inelastic scattering is also ignored. However, in practice, the variance is observed to have some dependence on thickness. When comparing data between amorphous Si samples of different thicknesses, Voyles *et al* [87] devised a correction procedure that allows normalized variance data to be compared between samples of different thickness. The correction is based on the assumption that the mean dark-field scattered intensity  $\langle I_{\text{DF}} \rangle$  can be approximated by an incoherent scattering equation of the type

$$\frac{\langle I_{\text{DF}} \rangle}{\langle I_0 \rangle} = C_1 \left( \frac{t}{\Lambda_{\text{DF}}} \right) \exp \left( -\frac{t}{\Lambda_{\text{DF}}} \right). \quad (36)$$

This predicts that the normalized variance changes as a function of  $t$  according to

$$V(t) = C_2 \frac{(t - t_0) \Lambda_{\text{DF}}^2}{t^2} \exp\left(\frac{2t}{\Lambda_{\text{DF}}}\right) \quad (37)$$

with two adjustable parameters  $C_2$  and  $t_0$ .  $\Lambda_{\text{DF}}$  (and  $C_1$ ) are estimated by fitting  $\langle I_{\text{DF}} \rangle$ . Ideally,  $t_0 = 0$ , but can be non-zero if the sample has extraneous layers on the surfaces, such as  $\text{SiO}_2$  layers on amorphous Si. FEM data of amorphous Si show that this empirical fit fails for  $t > 0.5\Lambda_{\text{DF}}$  [87]. The use of energy filters to collect only the elastic scattering contributions may improve the speckle contrast and extend the useable thickness. Clearly, when comparing variance data between similar samples, it is preferable if the samples have the same thickness.

### 2.5. Ordering at longer length scales: choice of radiation

The discussion presented so far has been focused on materials with ordering at near-atomic length scales, 0.5–3.0 nm. At present, electrons are usually the most appropriate probe at such length scales. However, electrons may not be the most appropriate choice for bulk self-assembled nanoscale materials and even mesoscale materials. The primary difficulty for electrons is their short scattering length, which limits sample thickness to perhaps 100 nm at most and less than 25 nm ideally. X-rays and even visible light may be more appropriate probes for aggregated materials.

The scattering theory presented here is a scalar theory and should work well for photon scattering, provided kinematical conditions prevail. Modifications will be necessary if the effects of photon polarization are important.

In principle, this discussion is also appropriate for neutron scattering. However, the ability to form finely focused neutron beams is limited at present.

## 3. Fluctuation electron microscopy of amorphous Si and Ge

### 3.1. Evidence of medium range order

FEM evolved as a technique that could extract microstructural information from amorphous tetrahedral semiconductor materials such as a-Si and a-Ge. Consequently, much of the experimental work to date has been concentrated on these systems. In this section we summarize the materials issues and the FEM results.

On the basis of pair correlation functions, obtained by diffraction, it had been determined that Si and Ge amorphous tetrahedral semiconductors could be classed as CRNs [66, 88, 89]. Calorimetric studies had shown that amorphous Ge experiences a structural relaxation when thermally annealed below the crystallization temperature [90]. As much as 50% of the heat of crystallization can be evolved. This heat evolution was originally noted for ion-implanted Ge and was interpreted as a relaxation of the framework. It was subsequently detected in varying degrees for other deposited amorphous semiconductor films [91]. Structural analysis revealed that the annealing led to a modest reduction in the amount of bond-angle disorder, resulting in an increase in short-range order. It had seemed reasonable to assume that there was a concomitant increase in medium-range ordering, although there were no experimental data to support such a claim.

FEM data for evaporated Ge [32], both before and after annealing *in situ* at 350 °C for 15 min, have been presented earlier in figures 5 and 6. The annealed data show a marked reduction in normalized variance. Modelling shows that the CRN models show few pronounced features in variance plots. Consequently, the data indicate that amorphous Ge evolves towards



the CRN structure upon annealing below the recrystallization temperature; that is, it becomes more disordered.

The effect of annealing on evaporated a-Si is less pronounced than it is for Ge. However, ion-implanted a-Si also shows relaxation to a more disordered state upon annealing [32, 35–37].

### 3.2. Thermodynamic instability of paracrystallites

This conclusion can be rationalized in terms of the paracrystallite model discussed earlier and depicted in figure 14. A granular, paracrystalline, structure on the scale of  $\sim 1.0$ – $2.0$  nm is formed during low temperature deposition. As the grains grow with random relative orientations an interfacial energy is incurred. It is a reasonable argument that a random network, with uniformly distributed strain energy and no inter-granular interfaces, will have a lower free energy. Upon annealing, the density of dangling bonds at the interfaces is reduced, improving the short range order and decreasing the overall strain energy, but also increasing the disorder in the framework. A simple model shows that there is a critical grain size,  $r_c$ , at which the energy is maximum [92]. For grain sizes  $r > r_c$ , there is no barrier to recrystallization (increasing the grain size  $r$ ). However, for  $r < r_c$ , there is a barrier to recrystallization and the free energy is reduced by transformation towards the metastable CRN, eliminating dangling bonds and interfacial energy.

A precise value for  $r_c$  is not known. The experiments on Ge show that there was a low density of  $\sim 10$  nm diameter crystallites present in the films, and these grains grew upon annealing. This places an upper bound on  $r_c \leq 10$  nm. Calculations using a simple thermodynamic model suggest that  $r_c \approx 3$ – $4$  nm for Si [92].

### 3.3. Influence of substrate temperature on growth

Substrate temperature at the time of deposition is also a factor controlling the extent of medium range order that is present in the film [93]. Figure 21 shows experimental electron diffraction and variance data from a-Si films grown at the five substrate temperatures  $T = 200, 250, 300, 350$  and  $440$  °C. The  $T = 200$ – $300$  °C samples show the characteristic pattern of diffraction from amorphous silicon, with peaks near  $q \approx 20$  and  $34$  nm $^{-1}$ . These peaks are not quite coincident with the positions of the first two diffraction peaks of a-Si, shown in figure 21(a). For substrate temperatures up to  $350$  °C, the second variance peak shifts to  $q \approx 35$  nm $^{-1}$  and lies approximately midway between the silicon 220 and 311 diffraction peaks and is presumably the sum of two broadened peaks. Part of the peak width in the variance data comes from the collection angular width of the objective aperture. The aperture is probably dominating the peak widths in the  $440$  °C variance data. All the variance data can be modelled as a sum of three Gaussians, as indicated by the solid lines in the figure. At the lower temperatures, two Gaussians seem to be sufficient.

The height of both the prominent variance peaks increases smoothly as substrate temperature increases from  $200$  to  $300$  °C. There is a reversal in the relative peak heights between  $200$  and  $250$  °C. The sample at  $440$  °C is polycrystalline, with a large variance that has been scaled by a factor of  $0.2$  to allow visual comparison with the other data. The variance at  $440$  °C also shows a shift in the position of the second peak to lower  $q$ , towards the cubic Si 220 reflection. A third peak appears as a shoulder near the 311 reflection position at  $q \approx 39$  nm $^{-1}$ . The variance of the  $T = 350$  °C data is intermediate between the amorphous and polycrystalline data, with the second peak position being shifted slightly towards lower  $q$ . Overall, the data imply a smooth, monotonic increase in medium range order as the substrate temperature is increased. The reversal in the peak heights also results from increased ordering because



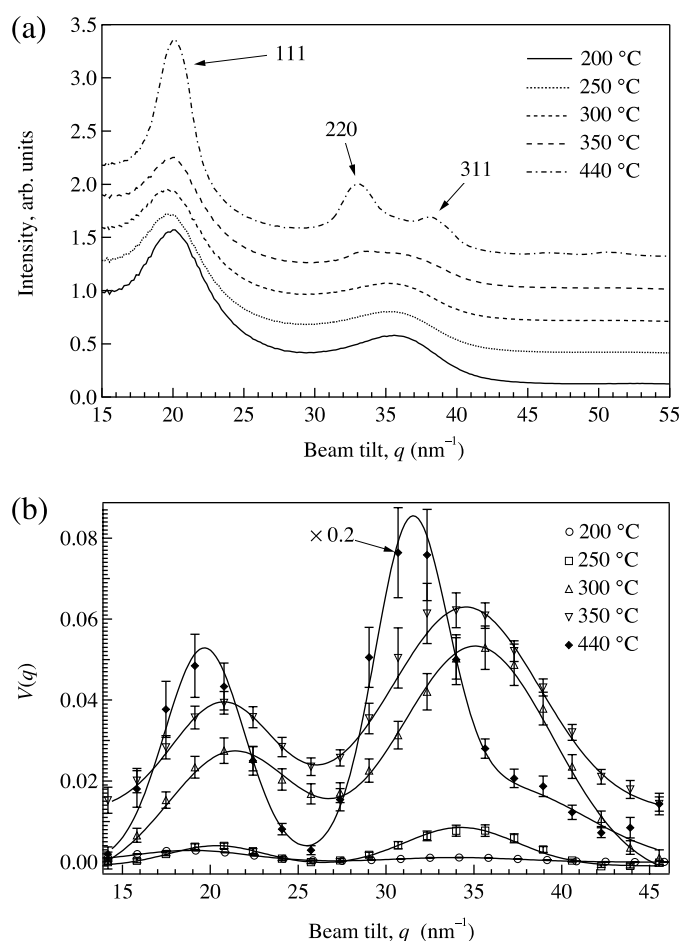


**Figure 21.** Diffraction and normalized variance data for evaporated Si films as a function of substrate temperature. (a) Electron diffraction. (b) Normalized variance. The continuous lines in the variance data represent a fit where each data set is modelled as the sum of 3 Gaussians [93]. The error bars represent the range in data over several measurements. The data are from [93].

diffraction from  $\{220\}$  planes is more sensitive to MRO, such as dihedral angle ordering, than diffraction from  $\{111\}$  planes [93]. This continuous evolution of ordering revealed by the FEM data is in contrast to the conclusions of Veprek *et al* [94–97]. Based on the abrupt appearance of peaks in the diffraction data, they concluded that the amorphous to polycrystalline transition is a discontinuous disorder–order phase transition.

### 3.4. Effects of paracrystallite size, shape and orientation

A comparison of the variance data for amorphous Ge (figure 6) with that for amorphous Si grown at low temperatures, 200 °C (figure 21(b)), shows that the relative heights of the two prominent peaks are reversed between these two materials. In Ge, the second peak is dominant, whereas for Si it is the first peak. With increasing substrate temperature the second peak grows faster and becomes dominant for Si. Based on our previous arguments, this observation suggests that the paracrystallite size for the Ge sample of figure 6 may be larger than the size

of the Si paracrystallites grown at the same temperature. However, there are additional issues that need to be considered. It has been shown that the 111 and 220 reflections are affected differently by disorder on the dihedral angles between two bonded, tetrahedrally coordinated, Si atoms [93]. The shape, as well as the size, of the ordered regions also plays a role in determining relative peak heights [83, 84], as well as any texturing in the material.

### 3.5. Amorphous silicon hydrogen materials

FEM studies of amorphous silicon–hydrogen (a-Si:H) photovoltaic materials show that paracrystalline MRO is present in these materials too, and is essentially independent of the preparation method and the hydrogen content [87, 98]. It is known that exposure to ultra-violet light reduces the photovoltaic efficiency of these devices [99]. *In situ* experiments, comparing the variance data before and after exposure to UV light, show that there is little change in variance  $V(q)$  upon exposure. A possible trend towards a reduction in variance was observed, but the effect was small [98]. The possibility that the reduction is induced by an annealing effect due to a temperature rise of  $\sim 50^\circ\text{C}$  during UV exposure has not been ruled out. It is clear that any changes in MRO associated with the Staebler–Wronski effect are, at best, subtle.

### 3.6. Electron beam damage of quartz

It has been tempting to speculate if silicate glasses also contain the equivalent of paracrystallites. In common with the amorphous tetrahedral semiconductors, the composition  $\text{SiO}_2$  of silicate glasses requires silicon to be 4-coordinated. However, silicate framework materials can explore a significantly larger number of structures—zeolites being an example. Many more thermodynamically plausible topologies are available to  $\text{SiO}_2$  [100]. Under electron beam irradiation, TEM images show that quartz ( $\text{SiO}_2$ ) amorphizes heterogeneously, developing disordered patches within a largely crystalline region [100]. The amorphous regions grow with increased dose, eventually merging. Cheng *et al* [51, 52] studied this phenomenon by depositing a suspension of crushed quartz sand onto a holey carbon film. Thin crystalline fragments were irradiated at doses of  $6 \times 10^6$  electrons/ $\text{s nm}^2$ . The dark field image variance of the amorphous regions showed no dependence on position away from the amorphous/crystal interface. This suggests that the freshly amorphized region near the interface has no residual ‘memory’ of its ordered crystalline origins. A factor that complicated the speckle variance analysis is the occurrence of nanometre-sized silicon particles in the amorphous matrix, which arise probably because of the preferential loss of small amounts of oxygen during irradiation. At the time of writing, silicate glasses are still a rich and open area for study by FEM.

## 4. Extension to other radiations

### 4.1. Fluctuation optical microscopy

The principles underpinning FEM are applicable to all types of coherent scattering processes provided the radiation can be focused to a width that is comparable with the length scale of the medium range order that is being investigated.

A FOM equivalent can be conceived for studying aggregated materials comprising building units that are larger than about  $1\ \mu\text{m}$ . Possible applications would be the study of macroscopic pore distributions in aerogels and starches. Time-dependent ordering of particle distributions in colloidal suspensions could also be studied. However, for the kinematical scattering limit that is assumed in this treatment, the optical path length through such suspensions will need to be short to minimize multiple scattering. Studies closely related to FOM have been conducted

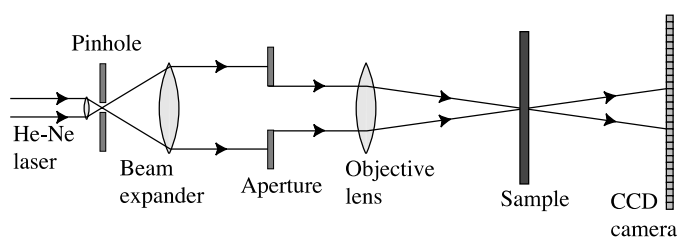


**Figure 22.** Schematic of a simple FOM set-up. The illumination source is a laser that first passes through a beam expander, then through an aperture before being focused by an objective lens onto a sample. The aperture diameter and objective lens focal length control the probe size. A CCD camera collects the scattered data. Typically, in such microscopes, it is the sample that is scanned. This figure is analogous to figure 8(c).

by Weitz *et al* [101, 102]. In those studies, time-dependent correlations in speckle patterns are measured to estimate diffusion time-constants. Figure 22 shows a simple outline of a FOM that is currently under construction at Arizona State University.

#### 4.2. Fluctuation x-ray microscopy

At the nano- and sub-micron length scales studies are underway to probe self-assembled materials using soft x-rays [63, 64]. Soft x-rays have energies in the range 30 eV–3.0 keV (40–0.4 nm wavelengths) and optical focusing techniques are well developed at these energies. Without any special optics, x-ray probes down to about 1  $\mu\text{m}$  width can be formed by using small pinholes that are positioned close to the sample, in the near-field so as to limit the probe-broadening effects of pinhole diffraction. In practice, pinhole sizes a little less than 1  $\mu\text{m}$  are readily available. Because of the practical difficulty of deflecting the x-ray beam in order to scan the probe, it is the sample that is scanned, as indicated schematically in figure 23(a). Alternatively, to achieve smaller probes, an x-ray zone plate [1, 2] with an order-sorting aperture can be used, as shown in figure 23(b). This STXM arrangement is equivalent to that for the fixed-beam STEM arrangement shown in figure 8(c). Probe sizes of  $\sim 20$  nm are achievable presently using such a system with soft x-rays [2]. The field of x-ray imaging is developing fast and x-ray probe sizes at the  $\sim 1$  nm level in the near future seem likely. Further, advanced optical techniques for focusing hard x-rays at energies of 20 keV are emerging [103, 105].

**4.2.1. FXM of latex sphere packing.** Early FXM experiments have studied thin films of aggregated latex spheres [63, 64]. Films are formed by drying droplets of colloidal suspensions of the spheres onto thin, x-ray transparent, amorphous SiN membranes. When dried slowly, the films are opalescent in visible light, indicating that they contain ordered, crystalline regions. When dried rapidly, the opalescence is subdued or suppressed, indicating disorder.

Figure 24 shows SEM micrographs taken of the surfaces of three dried films of monodisperse,  $277 \pm 3$  nm diameter, latex spheres. The film thicknesses are typically  $\sim 20$   $\mu\text{m}$ , as estimated by focusing on the upper and lower surfaces with an optical microscope. The extent of ordering in these films tends to increase with drying time. These samples are too thick for study by FEM. X-rays are a more appropriate probe for such materials. Sample A in figure 24(a) shows the film surface typical for a water-based suspension that dries slowly in air over about 15 min. The sample showed opalescence in white light. Sample B shown in figure 24(b) shows the film surface typical for a water/ethanol-based suspension that dries more quickly in air in about 3 min. Such samples are not noticeably opalescent. Sample C

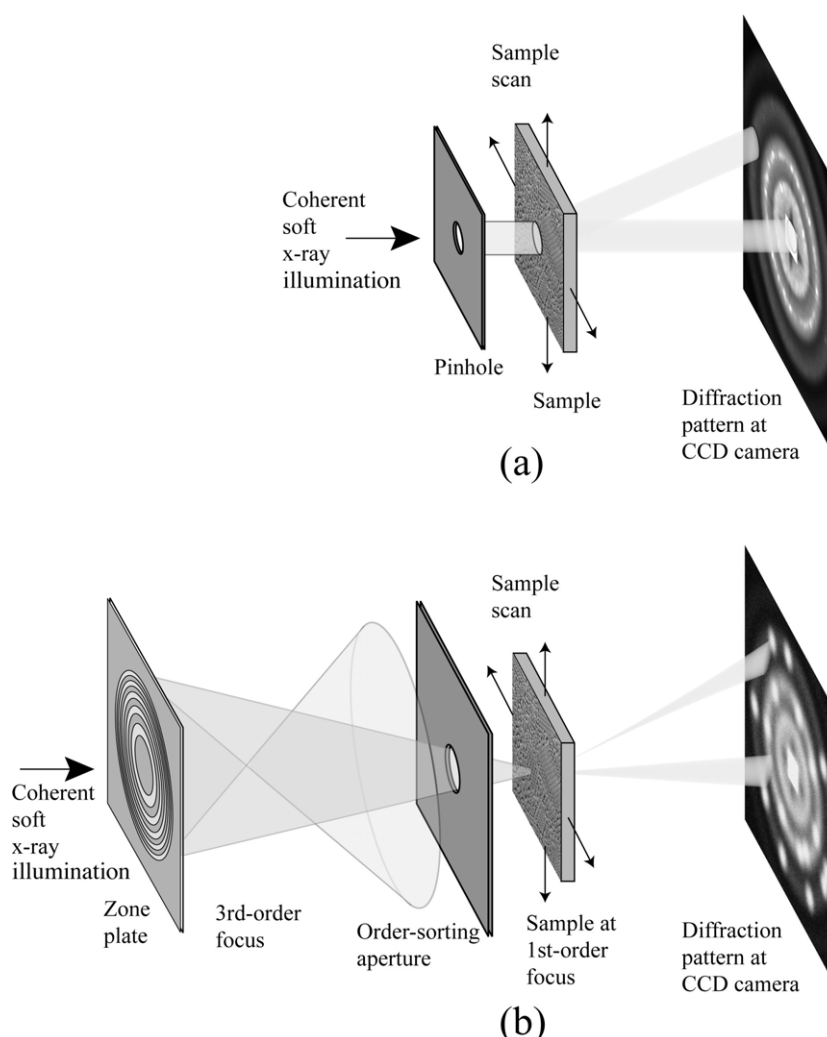


**Figure 23.** Schematic of a STXM. (a) With a pinhole defining the probe. (b) With a zone plate and order-sorting aperture defining the probe. It is usually simplest to scan the sample rather than the probe-forming x-ray optics.

in figure 24(c) was a water-based suspension that dried rapidly when pumped under vacuum over about 3 s, after standing in air for about 3 min. This latter sample was dried by a boiling action that produced a bubbled structure that subsequently flaked away in some areas producing rougher surfaces. No opalescence was observed, and there is little crystalline order evident in the roughened surface of sample C.

Figure 24(d) shows a sample similar to A with a crack revealing a side view of the material beneath the surface. The smooth ordered surface of the film belies the disorder that exists underneath. Clearly, relying on surface structural techniques such as SEM can be misleading, since they inadequately represent the internal structure underneath this surface skin.

These latex samples were studied by STXM using a series of pinholes at the 2-ID-B beamline at the APS synchrotron at the Argonne National Laboratory. The experimental configuration is depicted schematically in figure 23. Samples A and B were probed by an

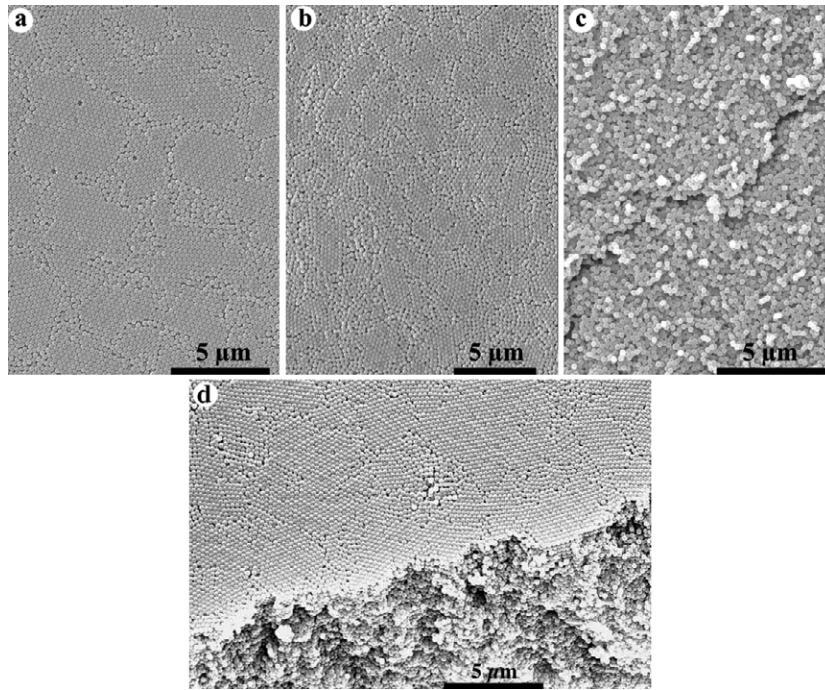


**Figure 24.** Scanning electron micrographs of the surfaces of films of 277 nm diameter latex spheres that were dried at different rates. (a) Air-dried water suspension. (b) Air-dried water-ethanol suspension. (c) Rapidly dried in vacuum. The extent of ordering at the surface decreases with decreasing drying time. (d) Air-dried suspension (as in (a)). A crack in the film reveals that the order visible within the surface 'skin' does not reflect the underlying disorder in the bulk of the film. Surface sensitive techniques such as SEM and AFM may overlook the bulk structure.

x-ray beam formed by a  $5.5\ \mu\text{m}$  pinhole that was placed in the near-field, about  $100\ \mu\text{m}$  in front of the sample, to minimize spreading of the probe by diffraction. The sample was scanned in  $2.75\ \mu\text{m}$  steps to form a 41 by 41 pixel square scan. The mean and normalized variance of the 1681 diffraction patterns are shown in figure 25.

A pronounced feature of the mean diffraction patterns is the set of broad rings corresponding to the spherical form factor  $F(q, R)$  for a sphere of radius  $R$ :

$$F(q, R) = \frac{4\pi R^3}{3} 3S(q) \left[ \frac{\sin(qR)}{(qR)^3} - \frac{\cos(qR)}{(qR)^2} \right]. \quad (38)$$

$S(q)$  is the scattering form factor for latex. The shot noise contribution has not been removed in the variance plots. Consequently, the shot noise associated with the intensity changes of the form factor remains visible in the variance.

The polycrystallinity of sample A is clearly evident in both the mean diffraction pattern, figure 25(a), and the normalized variance pattern, figure 25(b). The polycrystalline grain size is  $\sim 5\ \mu\text{m}$  corresponding to grains that are about 20 spheres wide and is well-matched to the nominal probe size formed by the pinhole.

Sample B is also polycrystalline, but with smaller grains  $\sim 2\ \mu\text{m}$  wide, about 7 spheres across. The SEM micrograph in figure 24(b) shows that the grains (at the surface at least) are significantly strained, a characteristic they share with the paracrystalline Si grains discussed earlier. The mean diffraction pattern (figure 25(c)) shows little visual evidence of the

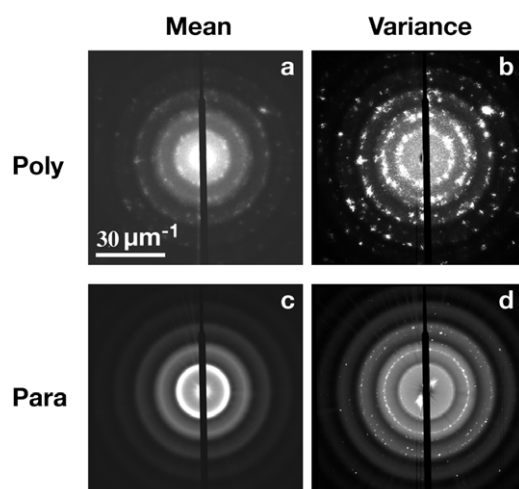


**Figure 25.** Mean and variance of samples A (a) and B (b) of figure 24, taken with a  $5.5\ \mu\text{m}$  pinhole. The mean diffraction pattern of sample B(c) is insensitive to the traces of order, the pattern being dominated by the rings arising from the spherical form factor. The variance (d) reveals the medium range order clearly, with sharp rings appearing.

polycrystallinity, whereas the normalized variance pattern (figure 25(d)) shows the order clearly as sharp rings on the second and third broad rings.

**4.2.2. Variable resolution FXM.** The scanning configuration lends itself well to the variable resolution mode of fluctuation microscopy, because it is easier to modify the probe size. Figure 26 shows mean diffraction and normalized variance data for the  $277\ \text{nm}$  latex sphere sample B (shown in figure 24(b)) for four pinhole diameters,  $0.8$ ,  $1.6$ ,  $5.5$  and  $10.0\ \mu\text{m}$ . The sizes were determined by measuring the angular radius  $\theta_{\text{Airy}}$  of the first zero of the Airy disc diffraction profile of the pinhole, with the sample removed. For radiation of wavelength  $\lambda$ , the pinhole diameter,  $D_{\text{ph}}$ , is found from  $D_{\text{ph}} = 1.22\lambda/\theta_{\text{Airy}}$ . For each pinhole size in figure 26, the left-hand side of each plot presents the mean diffraction pattern and the right-hand side presents the normalized variance. The vertical dark band is part of the shadow of the central beam stop. For each pinhole size, the sample was scanned as a  $61 \times 61$  array in steps of  $D_{\text{ph}}/2$  for optimal sampling. Consequently, the actual sample area that was probed decreases with decreasing pinhole size. For each pinhole size, the mean diffraction pattern does not show any crystalline diffraction features, whereas the normalized variance reveals the ordering clearly. As expected, the diffraction spot size increases inversely with the aperture size, reflecting the increasing beam angular divergence.

The sharp variance rings appear to have maximum intensity between the  $1.6$  and  $5.5\ \mu\text{m}$ . This suggests that the length scale of the characteristic medium range order lies within this range. This is generally consistent with the SEM scans of the surface structure. Better estimates of the length scale of the characteristic ordering could be obtained with finer step sizes in probe width.

The mean diffraction patterns in both figures 25 and 26 do show strong evidence of nearest-neighbour ordering. This appears as a strong bright ring on the outer edge of the central diffraction disc. This ring corresponds to the close-packed nearest-neighbour spacing of  $\sim 277\ \text{nm}$ , the sphere diameter. For face-centred cubic packing, this would correspond to



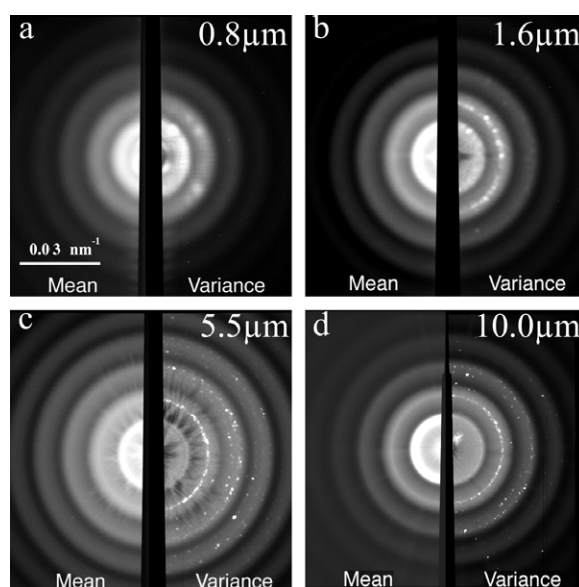


**Figure 26.** Mean and normalized variance data (left and right sides, respectively) from thin ( $\sim 20 \mu\text{m}$ ) films of 277 nm diameter latex spheres as a function of scanned pinhole size. The dark central band is the beam stop, which blocks the zero-order beam. (a)  $0.8 \mu\text{m}$  pinhole. (b)  $1.6 \mu\text{m}$ . (c)  $5.5 \mu\text{m}$  pinhole. (d)  $10.0 \mu\text{m}$  pinhole. The broad rings are due to the characteristic scattering factor of spheres, and the shot noise from these rings has not been removed from the variance data. The normalized variance diffraction data are more sensitive than the mean diffraction data to the presence of ordering.

the  $\{110\}$  planes. Interestingly, for the larger pinholes, 5.5 and  $10.0 \mu\text{m}$ , in figures 26(c) and (d), there is no significant variance on this nearest neighbour peak. In fact, there appears to be an overall reduction in normalized variance at the first nearest neighbour peak. An increased variance only shows up with the smaller 0.8 and  $1.6 \mu\text{m}$  pinholes (figures 26(a) and (b)), where smaller sample volumes are being probed. The second nearest neighbour spacings, and higher-order pairings, show persistent variance even for the larger pinholes. This is indicative of medium range order, but not of long range order. In the limit of perfect crystallinity, there would be no variance for these higher order peaks too.

**4.2.3. Dark-field x-ray microscopy.** The equivalent of incoherent dark-field images can be generated by masking the diffraction patterns at specified ranges of diffraction vectors. The integrated diffraction intensity collected by the mask at each probed point is displayed as a  $61 \times 61$  pixelated array. To generate the approximate equivalent of incoherent hollow cone dark field images, a set of masks can be created to select a range of diffraction vectors. Incoherent dark-field images from a sample that comprised two sizes of latex spheres are shown in figure 27. The spheres were 250 and 450 nm diameter mixed in a ratio of 5 : 1. It was hoped that this sample, upon drying, would generate a disordered dodecahedral sphere packing. SEM micrographs show that this did not happen, at least at the surface. The dark-field images were generated by thin annular masks centred at  $q = 0.021 \text{ nm}^{-1}$  (before the nearest neighbour ring),  $0.025 \text{ nm}^{-1}$  (on the averaged nearest neighbour ring),  $0.029 \text{ nm}^{-1}$  (the inside edge of the second broad form factor ring),  $0.031 \text{ nm}^{-1}$  (the outside edge of the second broad ring, which has an increased intensity) and  $0.045 \text{ nm}^{-1}$  (the dip after the second broad ring).

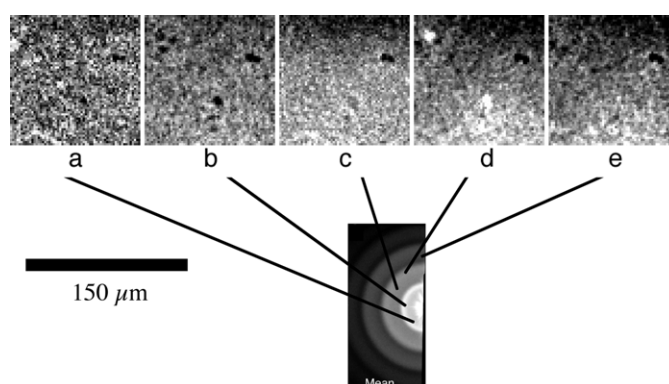


**Figure 27.** Reconstructed dark-field images of a latex sphere sample comprising a mixture of 250 and 450 nm diameter spheres that were mixed in the ratio 5 : 1. Images are 61 by 61 pixels, taken with the 5.5  $\mu\text{m}$  pinhole. The area measures 150 by 150  $\mu\text{m}$ . The masks were arc-shaped, spanning about 150° on each diffraction ring. (a) Inside the nearest neighbour ring,  $q = 0.021 \text{ nm}^{-1}$ . (b) On the nearest neighbour ring,  $q = 0.025 \text{ nm}^{-1}$ . (c) the inner rim of the first broad ring, excluding spots,  $q = 0.029 \text{ nm}^{-1}$ , (d) the outer rim of the first broad ring including spots,  $q = 0.032 \text{ nm}^{-1}$ , (e) dip after the first broad ring,  $q = 0.045 \text{ nm}^{-1}$ .

The speckle is reminiscent of that observed for amorphous Ge and Si (see figures 4 and 5). The bright regions scatter strongly into the mask, and clearly exhibit order. The dark regions scatter strongly out of the mask and are also likely to be ordered. For example, dark regions in figure 27(a) show up brightly in (d).

## 5. Future directions and concluding comments

### 5.1. Hardware and technique developments

The FEM evidence for paracrystallites in amorphous Si and Ge has spurred efforts to refine the sensitivity of RDFs for measuring MRO. Using his paracrystallite models, Kiehlinski and co-workers [104] have shown that by examining the decay length of the RDF,  $r[g(r) - 1]$ , as a function of pair separation  $r$ , where  $g(r)$  is the pair distribution function obtained by diffraction, the oscillatory decay lengths correlate well with the nominal paracrystallite size in the models. However, it remains to be seen if such decay lengths can be discriminated experimentally. Further, it is only by modelling the oscillatory nature of the decay that details of the structural topology can be obtained. However, the ongoing advances in the sensitivity of the synchrotron x-ray RDF technique [5, 6, 9, 10], and its modelling methods [8], are encouraging.

Thinking more about the medium-range future, a variety of exciting new technical avenues are attractive to explore in fluctuation microscopy, with correspondingly motivating applications. Certainly, fluctuation microscopy is not limited to electrons and x-rays. With attendant limitations on the momentum transfer that may be accessed with the wavelength of the radiation, and a suitably brilliant source to obtain the requisite coherent flux, the method could be extended to terahertz, infrared, visible and ultraviolet light, opening up the plethora of spectroscopies available in these regions of the electromagnetic spectrum. Apart from current technical limitations to focusing higher energy photons to the nanometre scale, there is also no reason why FXM cannot be extended to the hard x-ray region. Recent progress in the development of hard x-ray focusing optics are promising in this regard [105–107]. One might as well envision extension of fluctuation microscopy to particles other than electrons, such as



protons, neutrons and neutral atoms. Energetic protons, due to their very short wavelengths, potentially offer scattering at very high momentum transfer. Cold and thermal neutrons, which have wavelengths similar to those of soft and hard x-rays but which have a magnetic moment and large cross-section for hydrogenic materials, are uniquely suited to the study of magnetic materials and soft condensed matter [108, 109]. On the other hand, development of neutron fluctuation microscopy will be challenging due to the relatively low brilliance of today's neutron sources.

By contrast, third-generation synchrotron radiation sources provide enough coherent flux for x-ray fluctuation microscopy experiments due to their very high brilliance. By adapting the wide variety of contrast mechanisms now used in microscopy, scattering and spectroscopy in the x-ray region, one can imagine exquisitely sensitive fluctuation microscopy experiments with x-rays.

For example, one could enhance the contrast of selected sample constituents by tuning the incident x-ray energy near regions of anomalous dispersion at elemental absorption edges [110]. Judicious choice of the x-ray energy is a straightforward extension of basic x-ray fluctuation microscopy methodology and offers elemental and chemical-specific sample contrast near electronic resonances. Another property of waves—their polarization—could also be exploited. Although we have neglected to account for polarization in the foregoing theoretical treatment, both Rayleigh (transmission) and Fresnel (reflection) scattering are sensitive to the polarization of the incident radiation. Furthermore, many electronic and magnetic properties of matter couple to polarization of the probe radiation such as circular dichroism and other magnetic scattering effects in ferromagnetic materials [111]. Advantage could be taken of this sensitivity to polarization to study, for instance, antiferromagnetic ordering using linearly polarized x-rays or the magneto-optical Kerr effect hysteresis loops that probe the d-electronic state energies of the rare earth elements using circularly polarized x-rays [112].

Essential to fluctuation microscopy is control of the illumination spot size on the sample. With electrons this is easily accomplished by adjusting the electron optics in the column of a TEM as discussed in section 1.4. Similarly, the lens could be apertured in a scanning x-ray microscope configuration to change the illumination spot size on the sample. In particular, the apertures could be of different sizes along orthogonal axes to study orientationally-dependent ordering in the sample. Elliptical or rectangular apertures for x-ray fluctuation microscopy are feasible and would create probes whose width varies with azimuth. For isotropic samples, this would enable an azimuthally-dependent variable resolution mode. However, the 4-body scattering theory related to this mode has yet to be worked out.

More complex optical schemes may also be envisioned with electrons, x-rays and light, which would increase the sensitivity to ordering of weakly scattering sample domains. For example, energy filtration of the radiation scattered by the sample could enable isolation of the coherent (elastic) component from any incoherent (inelastic) components of the scattered radiation. In the x-ray regime, fluorescence and Compton scattering may pose non-negligible incoherent contributions to the total scattering cross-section of the sample [113].

In analogy to differential interference contrast methods used in visible light microscopy [114], two coherent focused probe spots could be directed onto the sample with variable separation and orientation. The radiation coherently scattered by the sample (speckle pattern) from each illumination spot will produce interference fringes at the detector whose spatial frequency depends inversely upon the spot separation. Information about the sample ordering on the scale of the probe separation and also its relative orientation will be encoded on the 'carrier wave' arising from the interfering spots in this heterodyne geometry. By applying variance analysis to a series of two-probe speckle measurements acquired as a function of

probe separation and orientation (e.g. displaced first vertically then horizontally with respect to the sample), one could map medium range order as a function of relative correlation length and orientation of the sample domains. The principal advantages of this approach over the homodyne (single-spot) methods described here are reduced background (only the fringes resulting from the interference between the radiation scattered from each illuminated point need be recorded) and continuous controllability of the correlation length probed in the sample by simply changing the spot separation.

On the theoretical front, considerable work lies ahead to treat properly the effects of multiple scattering by thick samples on fluctuation microscopy data. Rather than address this important point further here, we merely point out that multiple scattering poses the main obstacle to the study of specimens thicker than  $\sim 300$  nm using electrons and a few microns using visible light. For x-rays, the Born approximation is largely valid up to sample thicknesses of many microns.

Higher order statistical moments may offer additional information. The authors routinely examine the third and fourth moments (skew and kurtosis) of the intensity distributions in FXM studies. These higher order moments also reveal structural fluctuations, and in some instances appear to be more sensitive than simply the variance. However, more theoretical work is needed to establish what this means at the structural level.

So far, this review has only addressed spatial correlations. In principle the time ( $t$ ) domain could also be explored in a fluctuation microscopy experiment that probes the variance  $V(\mathbf{q}, K_{\text{ap}}, t)$ , i.e. a complete picture of not only the spatial but also the temporal correlations in the sample. This extension could be viewed as combining the capabilities of photon correlation spectroscopy with those of conventional fluctuation microscopy. Adding sensitivity to temporal correlations opens the door to the investigation of sample dynamics such as temperature and solvent dependent critical fluctuations near phase transitions in liquid crystals, order-disorder fluctuations in materials such as polymer melts and bimetallic alloys and potentially non-equilibrium fluctuations in low-dimensionality materials such as glasses and gels. While experimentally formidable to combine the temporal and spatial domains in this way, visible photon correlation spectroscopy has been used for many years to study aerosols, colloids and dispersions with as high as nanosecond time resolution. X-ray photon correlation spectroscopy techniques, though more recent, offer a time resolution extending to the millisecond regime with a strong potential for reaching shorter time scales using fast-readout cameras. The advent of free-electron x-ray laser sources in the next few years at several laboratories worldwide promises an unprecedented increase in peak brilliance as well as a time resolution extending to the femtosecond regime [115].

## 5.2. Disordered materials from the nanoscale to the mesoscale

Amorphous silicon and germanium have been the focus of the discussion on materials in this review because these systems have been well explored by FEM. The introduction discusses other materials that are being actively examined by other groups using FEM. Clearly, these examples do not exhaust the interesting materials systems that can be examined by fluctuation microscopy. Here we will describe briefly a shortlist of additional materials systems with important open scientific questions that might be fruitfully addressed by some form of fluctuation microscopy.

Chalcogenide glasses, particularly materials such as  $\text{Ge}_2\text{Sb}_2\text{Te}_5$ , have attracted much attention recently as phase change memory alloys for C-RAM devices [116, 117]. Small volumes of material can be rapidly switched between crystalline and amorphous states by heating. The amorphous state has low reflectance and high resistivity and can be induced

by cooling rapidly or by applying a threshold electric field to the crystalline phase. The polycrystalline phase has high reflectivity and low resistance and is obtained from the amorphous phase by heating and cooling more slowly. Such materials are easily integrated into existing silicon technology and offer much promise as potential non-volatile computer memories. The structural nature of the amorphous phase is unknown, and it is not known if there are any 'fatigue' issues related to repeated switching (phase changing) of thin films.

In glasses, it is known that just above the glass transition temperature  $T_g$  a number of physical processes are activated, likely involving structural rearrangements, with long time constants [118, 119]. Speckle studies just above and below  $T_g$  in the TEM may provide key insights into these processes. Such studies would undoubtedly require speckle analysis in both the spatial and temporal domains. For the TEM case, a glassy system with a low  $T_g$  would be desirable.

Fluctuation microscopy work to date has been focused on the search for traces of structural order within largely disordered samples, i.e. at the lower left corner of the order–disorder diagram in figure 1. It should likewise be possible to exploit the sensitivity of the variance (or higher-order statistical moments) in fluctuation microscopy data to measure the presence of trace quantities of disorder in otherwise perfect crystals (i.e. near the right corner of figure 1), such as rare dislocations in protein crystals, compositional disorder (plus concomitant strain) in relaxor ferroelectric materials and crystal defects due to radiation damage.

Along similar lines, some magnetic framework materials have crystalline lattices that frustrate antiferromagnetic ordering of spins [120]. X-ray scattering (and particularly neutron scattering) is sensitive to magnetic spin and may be able to address the issue of medium range ordering if present. Spin polarized electron microscopy [121], although by no means a mainstream technique, may also be able to glean details of any magnetic ordering from spin-filtered image speckle.

Ordering in polymers is a subject of great interest [122]. Because of their vulnerability to electron beam damage, high resolution TEM is difficult, and FEM (at least as described in this paper) may very well be impractical. However, at longer length scales, block co-polymers and other types of soft materials can exhibit a fluid-like disorder on the molecular scale and a high degree of order at longer length scales. This complex dual order–disorder structure can endow block copolymers with useful properties. FXM holds much promise for examining the disordered phases of these materials at the longer length scales.

Mesoporous materials, such as silicates formed from gels containing large organic molecules, can exhibit similar disorder at atomic length scales, while possessing ordered pore structures. However, many useful silicate materials possess disordered mesoscale pore systems. A prime example is the low- $K$  dielectric materials that are being developed for high density computer chips. The materials need to be thin, support a framework of open space and yet contain no contiguous open channels that might permit short circuits through diffusion of conducting material. Both FEM and FXM are viable techniques for examining the disorder of the cavities.

This approach can be used for the exploration of medium range order and the subtle spatial structural changes in soft matter such as polymers, biological systems, self-assembled nanostructures, nanocomposite and hybrid materials. For example, it can be used to study nucleation and order–disorder phase transition in these materials. It will provide the information about ordering changes and other detailed structure information that help us to understand the mechanisms of order–disorder transition. It may lead to control of ordering, which is important in developing specific structures tailored for particular applications. This approach also can be used to study nanowire arrays, semiconductor quantum dot arrays and magnetic materials.

The nucleation and growth of zeolites is a subject of great interest to the catalyst and fine chemicals industries. A precise and definitive description of gel formation, seed nucleation and subsequent growth, has proved elusive. Fedeyko and co-workers [123] recently demonstrated that RDFs of zeolite growth within colloidal gel particles could be obtained from synchrotron x-ray diffraction, showing sensitively the onset of crystal growth. It appears reasonable to speculate that a similar experimental set-up might allow speckle measurements to be made that could reveal more structural details of the nucleation stages. Given the short length scales involved,  $\sim 1$  nm, a hard x-ray set-up might be desirable.

Order and disorder of molecules within lipid and protein biomembranes and Langmuir–Blodgett films is perhaps readily examined by conventional TEM methods, since these are, for the most part, thin two-dimensional structures. However, Langmuir–Blodgett films can be stacked to form multilayers, such as quantum dot arrays. In such cases, these assemblies are frequently too thick for TEM. Such materials built from fragile layers may exhibit anisotropic disorder, with different length scales for intralayer and interlayer directions.

### 5.3. Conclusions

Fluctuation microscopy has existed as a technique for about a decade. Its sensitivity to medium range order within materials, when compared with either diffraction or imaging methods alone, has attracted the active interest of a number of groups for studying a variety of disordered materials, particularly as a transmission electron microscopy technique.

It is clear that fluctuation microscopy as a technique is still evolving, and with a growing base of research groups using the technique. The technique evolution is driven mainly by advances in our understanding of higher order correlation functions. 4-body correlations (or pair–pair distributions) are not intuitive concepts compared with the simpler pair-correlations that underpin pure diffraction and imaging theory. The ideas leading to the dual-spot heterodyne geometry proposed earlier (section 5.1) represent a potentially powerful experimental tool for determining pair–pair correlations more directly.

We anticipate exciting new results and developments in the short- to medium-range future, particularly in the area of x-ray imaging of nanoscale materials.

### Acknowledgments

MMJT wishes to thank Arizona State University and the Argonne National Laboratory for providing support during the writing of this paper.

### References

- [1] Kirz J 1974 *J. Opt. Soc. Am.* **64** 301
- [2] Attwood D T 1999 *Soft X-rays and Extreme Ultraviolet Radiation: Principles and Applications* (Cambridge: Cambridge University Press)
- [3] Ossi P M 2003 *Disordered Materials: an Introduction* (Berlin: Springer)
- [4] Warren B E 1959 *X-ray Diffraction* (Reading: Addison-Wesley)
- [5] Billinge S J L 1998 *Local Structure from Diffraction* ed S J L Billinge and M F Thorpe pp 137–56
- [6] Proffen T and Billinge S J L 1999 *J. Appl. Crystallogr.* **32** 572
- [7] Moss S C and Graczyk J F 1969 *Phys. Rev. Lett.* **23** 1167
- [8] Levashov V A, Billinge S J L and Thorpe M 2005 *Phys. Rev. B* **72** 024111
- [9] Petkov V, Billinge S J L, Shastri S D and Himmel B 2001 *J. Non-Cryst. Solids* **293–295** 726
- [10] Petkov V, Qadir D and Shastri S D 2004 *Solid State Commun.* **129** 239
- [11] Zachariasen W H 1932 *J. Am. Chem. Soc.* **54** 3841

- [12] Freeman L A, Howie A, Mistry A B and Gaskell P H 1976 *The Structure of Non-Crystalline Materials* ed P H Gaskell (London: Taylor and Francis) pp 245–51
- [13] Howie A 1978 *J. Non-Cryst. Solids* **31** 41
- [14] Krivanek O L, Gaskell P H and Howie A 1976 *Nature* **262** 454
- [15] Cheng S L, Lin H H, TeHe J H, Chiang T F, Yu C H, Chen L J, Yang C K, Wu D Y, Chien S C and Chen W C 2002 *J. Appl. Phys.* **31** 910
- [16] Galvez A, Herlin-Boime N, Reynaud C, Clinard C and Rouzaud J-N 2002 *Carbon* **40** 2775–89
- [17] Bucheli T D, Kukulska Z, Andersson M, Largeam C, Gustafsson Ö, Rouzaud J-N, Reddy C M and Eglington 2001 Evaluation of a protocol for the quantification of black carbon in sediments *Global Biogeochem. Cycles* **15** 881–90
- [18] Oberlin A 1989 High-resolution studies of carbonization and graphitization *Chemistry and Physics of Carbon* vol 22 (New York: Dekker)
- [19] Rouzaud J-N, Skrzypczak A, Bonal L, Derenne S, Quirico E and Robert F 1977 *Proc. Lunar and Planetary Science XXXVI (Houston, USA)* vol 21B (London: Institute of Physics) pp 279–82
- [20] Dainty J C 1975 *Laser Speckle and Related Phenomena* ed J C Dainty (New York: Springer) pp 1–7
- [21] Goodman J W 1975 *Laser Speckle and Related Phenomena* ed J C Dainty (New York: Springer) pp 60–68
- [22] Fan G Y and Cowley J M 1988 *Ultramicroscopy* **24** 49
- [23] Rudee M L and Howie A 1972 *Phil. Mag.* **25** 1001
- [24] Chaudhari P, Graczyk J F and Charbneau H P 1972 *Phys. Rev. Lett.* **29** 425–29
- [25] Howie A, Krivanek O L and Rudee M L 1973 *Phil. Mag.* **27** 235
- [26] Treacy M M J and Gibson J M 1993 *Ultramicroscopy* **52** 31
- [27] Krakow W and Howland L A 1976 *Ultramicroscopy* **2** 53
- [28] Gibson J M and Howie A 1978 *Chem. Scr.* **14** 109
- [29] Howie A 1978 *J. Non-Cryst. Solids* **31** 41
- [30] Gibson J M 1978 Investigations of amorphous structures *PhD Thesis* Cambridge University, Cambridge, UK
- [31] Cochran W 1973 *Phys. Rev. B* **8** 623
- [32] Gibson J M and Treacy M M J 1997 *Phys. Rev. Lett.* **78** 1074
- [33] Treacy M M J and Gibson J M 1996 *Acta Crystallogr. A* **52** 212
- [34] Gibson J M and Treacy M M J 1998 *J. Non-Cryst. Solids* **231** 99
- [35] Gibson J M, Cheng J-Y, Voyles P M, Treacy M M J and Jacobson D C 1999 *Microstructural Processes in Irradiated Materials* vol 540, ed S J Zinkle *et al* (Warrendale: Materials Research Society) pp 27–32
- [36] Gerbi J E, Voyles P M, Treacy M M J, Gibson J M, Chen W C, Hauser B J and Abelson J R 2001 *Amorphous and Heterogeneous Silicon-Based Thin Films—2001* vol 664, ed M Stutzmann *et al* (Warrendale: Materials Research Society) pp A27.3.1–6
- [37] Gerbi J E, Voyles P M, Treacy M M J, Gibson J M and Abelson J R 2003 *Appl. Phys. Lett.* **82** 3665
- [38] Voyles P M and Abelson J R 2003 *Solar Energy Mater. Solar Cells* **78** 85
- [39] Chen X, Gibson J M, Sullivan J, Friedman T and Voyles P M 2001 *Microcrystalline and Nanocrystalline Semiconductors—2000* vol 663, ed P M Fauchet *et al* (Warrendale: Materials Research Society) pp F14.40.1–F14.40.6
- [40] Chen X, Gibson J M, Sullivan J and Friedmann T 2001 *Nanotubes, Fullerenes, Nanostructured and Disordered Carbon* vol 675, ed J Robertson *et al* (San Francisco, CA: Materials Research Society) pp W12.1.1–W12.1.6
- [41] Chen X, Sullivan J P, Friedmann T A and Gibson J M 2004 *Appl. Phys. Lett.* **84** 2823
- [42] Johnson J A, Woodford J B, Chen X, Anderson J, Erdemir A and Fenske G F 2004 *J. Appl. Phys.* **95** 7765
- [43] Stratton W G, Hamann J, Perepezko J H and Voyles P M 2004 *Amorphous and Nanocrystalline Metals* vol 806, ed R Busch *et al* (Boston: Materials Research Society) pp MM9.4 1–6
- [44] Stratton W G, Voyles P M, Hamann J and Perepezko J H 2004 *Microsc. Microanal.* **10**(Suppl. 2) 788
- [45] Stratton W G, Hamann J, Perepezko J H, Voyles P M, Khare S V and Mao X 2005 *Appl. Phys. Lett.* **86** 141910
- [46] Li J, Gu X and Hufnagel T C 2001 *Microsc. Microanal.* **7** (Suppl. 2: Proceedings) 1260
- [47] Li J, Gu X and Hufnagel T C 2003 *Microsc. Microanal.* **9** 509
- [48] Hufnagel T C, Fan C, Ott R T, Li J and Brennan S 2002 *Intermetallics* **10** 1163
- [49] Chen X, Sullivan J, Barbour C, Johnson C, Zhou G and Yang J 2002 *Spatially Resolved Characterization of Local Phenomena in Materials and Nanostructures* vol 738, ed J Piqueras *et al* (Boston: Materials Research Society) pp G1.4.1–G1.4.6
- [50] Ho M-Y *et al* 2003 *J. Appl. Phys.* **93** 1477
- [51] Cheng J-Y, Treacy M M J and Keblinski P J 2003 *Amorphous and Nanocrystalline Silicon-Based Films—2003* vol 762 ed J R Abelson *et al* (Boston: Materials Research Society) pp A5.18.1–6
- [52] Cheng J-Y, Treacy M M J, Keblinski P J and Gibson J M 2004 *J. Appl. Phys.* **95** 7779
- [53] Hobbs L W 2003 private communication

- [54] Fan G Y and Cowley J M 1985 *Ultramicroscopy* **17** 345
- [55] Cowley J M 2001 *J. Electron Microsc.* **50** 147
- [56] Cowley J M 2002 *Ultramicroscopy* **90** 197
- [57] Rodenburg J M 1985 *Inst. Phys. Conf. Ser. No 78* (London: Institute of Physics) p 103
- [58] Voyles P M and Muller 2002 *Ultramicroscopy* **93** 147
- [59] Gibson J M, Treacy M M J and Voyles P M 2000 *Ultramicroscopy* **83** 169
- [60] Treacy M M J, Gibson J M and Voyles P M unpublished
- [61] McBride W and Cockayne D J H 2003 *J. Non-Cryst. Solids* **318** 233
- [62] McBride W E 1999 *PhD Thesis* University of Sydney
- [63] Fan L, McNulty I, Paterson D J, Treacy M M J and Gibson J M 2005 *Neutron and X-Ray Scattering as Probes of Multiscale Phenomena* vol 840, ed S R Bhatia *et al* (Warrendale: Materials Research Society) pp Q6.7.1–6
- [64] Fan L, McNulty I, Paterson D J, Treacy M M J and Gibson J M 2005 *Nucl. Instrum. Method. B* **238** 196–99
- [65] Born M and Wolf E 1999 *Principles of Optics: Electromagnetic Theory of Propagation, Interference and Diffraction of Light* (Cambridge: Cambridge University Press)
- [66] Polk D E 1971 *J. Non-Cryst. Solids* **5** 365
- [67] Polk D E and Boudreaux D S 1973 *Phys. Rev. Lett.* **31** 92
- [68] Duffy M G, Boudreaux D S and Polk D E 1975 *J. Non-Cryst. Solids* **15** 435
- [69] Wooten F, Winer K and Weaire D 1987 *Solid State Phys.* **40** 1
- [70] Wooten F, Winer K and Weaire D 1985 *Phys. Rev. Lett.* **54** 1392
- [71] Biswas R and Hamman D R 1987 *Phys. Rev. B* **36** 6434
- [72] Biswas R, Grest G S and Sokoulis C M 1989 *Phys. Rev. B* **39** 5101
- [73] Biswas R, Kwon I, Bouchard A M, Sokoulis C M and Grest G S 1989 *Phys. Rev. B* **39** 5101
- [74] Keblinski P, Phillpot S R, Wolf D and Gleiter H 1996 *Phys. Rev. Lett.* **77** 2965
- [75] Keblinski P, Phillpot S R, Wolf D and Gleiter H 1997 *Phys. Lett. A* **226** 205
- [76] Keblinski P, Phillpot S R, Wolf D and Gleiter H 1997 *Acta Mater.* **40** 987
- [77] Keblinski P, Phillpot S R, Wolf D and Gleiter H 1997 *J. Am. Ceram. Soc.* **80** 717
- [78] Hosemann R and Bagchi S N 1962 *Direct Analysis of Diffraction by Matter* (Amsterdam: North-Holland)
- [79] Cowley J M 1981 *Diffraction Studies on Non-Crystalline Substances* vol 13 ed I Hargittai and W J Orville-Thomas (Amsterdam: Elsevier) pp 848–91
- [80] Biswas P, Atta-Fynn R and Drabold D A 2004 *Phys. Rev. B* **69** 195207
- [81] Biswas P, Tafen D and Drabold D A 2005 *Phys. Rev. B* **71** 054204
- [82] Dash R K, Voyles P M, Gibson J M, Treacy M M J and Keblinski P 2003 *J. Phys.: Condens. Matter* **15** S2425
- [83] Khare S V, Nakhmanson S M, Voyles P M, Keblinski P and Abelson J R 2004 *Appl. Phys. Lett.* **85** 745
- [84] Khare S V, Nakhmanson S M, Voyles P M, Keblinski P and Abelson J R 2004 *Microsc. Microanal.* **10**(Suppl. 2) 820
- [85] Treacy M M J and Gibson J M 1977 *Inst. Phys. Conf. Ser. No 153* ed J M Rodenberg (London: Institute of Physics) pp 433–436
- [86] Iwai T, Gibson J M, Voyles P M and Oono Y 1999 *Phys. Rev. B* **60** 191
- [87] Voyles P M, Treacy M M J, Gibson J M, Jin H C and Abelson J R 2001 *Amorphous and Heterogeneous Silicon Thin Films 2000* ed R W Collins *et al* (Warrendale: Materials Research Society) *Mater. Res. Soc. Symp. Proc.* **609** A2.4.1–A2.4.6
- [88] Temkin R J, Paul W and Connell G A N 1973 *Adv. Phys.* **22** 581
- [89] Connell G A N and Temkin R J 1974 *Phys. Rev. B* **9** 5323
- [90] Donovan E P, Spaepen F, Turnbull D, Poate J M and Jacobson D C 1985 *J. Appl. Phys.* **57** 1795
- [91] Avilez R R D, Clevenger L A and Thompson C V 1989 *J. Mater. Res.* **4** 1057
- [92] Voyles P M, Treacy M M J and Gibson J M 2001 *New Methods, Mechanisms and Models of Vapor Deposition* ed H N G Wadley *et al* (Warrendale: Materials Research Society) *Mater. Res. Soc. Symp. Proc.* **616** 47–52
- [93] Voyles P M, Gerbi J E, Treacy M M J, Gibson J M and Abelson J R 2001 *Phys. Rev. Lett.* **86** 5514
- [94] Veprek S, Iqbal Z, Oswald H R, Sarott F-A, Wagner J J and Webb A P 1981 *Solid State Commun.* **39** 509
- [95] Veprek S, Iqbal Z and Sarott F-A 1982 *Phil. Mag. B* **45** 137
- [96] Veprek S, Iqbal Z, Oswald H R, Sarott F-A and Wagner J J 1981 *J. Phys. Coll.* **42** 251
- [97] Sarott F-A, Iqbal Z and Veprek S 1982 *Solid. State Commun.* **42** 465
- [98] Gibson J M, Treacy M M J, Voyles P M, Jin H-C and Abelson J R 1998 *Appl. Phys. Lett.* **73** 3093
- [99] Staebler D L and Wronski C R 1977 *Phys. Rev. Lett.* **31** 292
- [100] Hobbs L W, Jesurum C E, Pulim V and Berger B 1998 *Phil. Mag. B* **78** 679
- [101] Pine D J, Weitz D A, Chaikin P M and Herbolzheimer E 1980 *Phys. Rev. Lett.* **60** 1134
- [102] Weitz D A, Pine D J, Pusey D N and Tough R J A 1989 *Phys. Rev. Lett.* **63** 1747
- [103] Shastri S D 2004 *J. Synchrotron Radiat.* **11** 150

- [104] Bodapati A, Treacy M M J, Falk M, Kieffer J and Keblinski P 2005 *J. Non-Cryst. Solids* at press
- [105] Maser J, Stephenson G B, Vogt S, Yun W, Macrander A, Kang H C, Liu C and Conley R 2004 *Proc. SPIE* **5539** 185
- [106] Kang H C, Stephenson G B, Liu C, Conley R, Macrander A T, Maser J, Bajt S and Chapman H N 2005 *Appl. Phys. Lett.* **86** 151109
- [107] Liu C, Conley R, Macrander A T, Maser J, Kang H C, Zurbuchen M and Stephenson G B 2005 *J. Vac. Sci. Technol.* A at press
- [108] Hicks T J 1995 *Neutron Scattering in Condensed Matter* ed S W Lovesey and W Mitchell (Oxford: Oxford University Press)
- [109] Hicks T J 1996 *Adv. Phys.* **45** 243
- [110] Retsch C C and McNulty I 2001 *Phys. Rev. Lett.* **87** 077401
- [111] Thole B T, Carra P, Sette F and van der Laan G 1992 *Phys. Rev. Lett.* **68** 1943
- [112] Carra P, Thole B T, Altarelli M and Wang X 1993 *Phys. Rev. Lett.* **70** 694
- [113] Thompson A *et al* 2001 *X-ray Data Booklet* (Berkeley: Lawrence Berkeley National Laboratory)
- [114] Allen R D, Allen N S and Travis J L 1981 *Cell Motil.* **1** 291
- [115] Liu Y, Wang X J, Cline D B, Babzien M, Fang J M, Gallardo J, Kusche K, Pogorelsky I, Skaritka J and van Steenbergen A 1998 *Phys. Rev. Lett.* **80** 4418
- [116] Ovshinsky S R 1968 *Phys. Rev. Lett.* **21** 1450
- [117] Lai S 2003 *IEDM Technical Digest* pp 255–258
- [118] Walther L E, Israeloff N E, Russell E V and Gomariz H A 1998 *Phys. Rev. B* **57** 112
- [119] Russell E V, Israeloff N E, Walther L E and Gomariz H A 1998 *Phys. Rev. Lett.* **81** 1461
- [120] Bramwell S T and Gingras M J *Science* **294** 1495 2001
- [121] Bauer E 1994 *Rep. Prog. Phys.* **57** 895
- [122] Hadjichristidis N, Pispas S and Floudas G 2003 *Block Copolymers: Synthetic Strategies, Physical Properties, and Applications* (New York: Wiley)
- [123] Fedeyko J M, Rimer J D, Lobo R F and Vlachos D G 2004 *J. Phys. Chem. B* **108** 12271